

DMYTRO DANILIAN

Photocatalytic materials for
water treatment and
antimicrobial applications



DMYTRO DANILIAN

Photocatalytic materials for water treatment
and antimicrobial applications



UNIVERSITY OF TARTU

Press

Institute of Physics, Faculty of Science and Technology, University of Tartu,
Estonia

The Dissertation was admitted on June 20, 2024, in partial fulfilment of the requirements for the degree of Doctor of Philosophy in materials science, and allowed for defence by the Scientific Council on Materials Science of the Faculty of Science and Technology of the University of Tartu.

Supervisors: Dr. Vambola Kisand, Institute of Physics, University of Tartu
Dr. Rainer Pärna, Institute of Physics, University of Tartu
Prof. Angela Ivask, Institute of Molecular and Cell Biology,
University of Tartu

Opponent: Dr. Andrei Kanaev, CNRS, Université Sorbonne Paris Nord

Commencement: August 26, 2024 at University of Tartu, Tartu, Estonia

Estonian Research Council Grants (EAG20, PRG1496, COVSG2), Estonian Centre of Excellence in Research projects “Advanced materials and high-technology devices for sustainable energetics, sensorics and nanoelectronics” TK141 and “Center of Excellence in Sustainable Green Hydrogen and Energy Technologies” TK210, University of Tartu Development Fund (grant PLTFYARENG53), Graduate School of Functional materials and technologies receiving funding from the European Regional Development Fund in University of Tartu, Estonia (project code 2014–2020.4.01.16–0027). Research related to pesticide degradation was also supported by Estonian Research Council grant MOBTP145.

The research was partly conducted using the NAMUR+ core facility funded by projects “Center of Nanomaterials Technologies and Research” (2014–2020.4.01.16-0123) and TT13. Experiments were also carried out at the FinEstBeAMS beamline, which operation costs were partially supported within the MAX-TEENUS project (grant no. 2014–2020.4.01.20-0278) by the ERDF and TT20.

ISSN 2228-0928 (print)
ISBN 978-9916-27-594-8 (print)
ISSN 2806-2574 (pdf)
ISBN 978-9916-27-595-5 (pdf)

Copyright: Dmytro Danilian, 2024

University of Tartu Press
www.tyk.ee



European Union
European Regional
Development Fund



Investing
in your future

TABLE OF CONTENTS

LIST OF PUBLICATIONS	7
AUTHOR'S CONTRIBUTION.....	8
ABBREVIATIONS AND SYMBOLS	9
1. INTRODUCTION.....	10
2. LITERATURE REVIEW.....	11
2.1 Photocatalysis	11
2.2 Photocatalyst-driven hydrophilicity	13
2.3 Photocatalyst materials in antimicrobial applications.....	14
2.4 Photocatalysis-based water treatment	16
2.5 Key techniques for the characterisation of photocatalysts.....	17
2.5.1 X-ray photoelectron spectroscopy.....	17
2.5.2 Ultraviolet-visible spectroscopy.....	19
2.5.3 X-ray diffraction.....	20
2.5.4 Scanning transmission electron microscopy	20
3. MOTIVATION AND AIM OF THE WORK.....	22
4. MATERIALS AND METHODS	25
4.1 Photocatalyst synthesis	25
4.1.1 The synthesis of TiO ₂ with CuFe ₂ O ₄ -Fe ₂ O ₃	25
4.1.2 Synthesis of nano-ZnO and nano-ZnO/Ag.....	25
4.2 Surface and coating preparation.....	26
4.2.1 Nano-ZnO and nano-ZnO/Ag in acrylic matrix on plywood.....	26
4.2.2 ZnO in acrylic matrix on stainless steel	26
4.2.3 Commercially available glass Pilkington SaniTise™ and BIOCLEAN®	28
4.3 Characterisation of photocatalytic materials and surfaces	28
4.3.1 X-ray photoelectron spectroscopy.....	28
4.3.2 Scanning transmission electron microscopy with energy-dispersive X-ray spectroscopy	28
4.3.3 UV-Vis absorbance	29
4.3.4 Contact angle measurements of surfaces	29
4.3.5 Other characterisation techniques	29
4.4 Photocatalytic analysis of surfaces	31
4.5 Photocatalytic degradation of pesticide 2,4-D	31
5. RESULTS AND DISCUSSION	32
5.1 Reusable magnetic photocatalyst for water purification (Paper I).....	32
5.2 ZnO and ZnO/Ag based photocatalytic coatings	39
5.2.1 Nano-ZnO and nano-ZnO/Ag based photocatalytic coatings (Paper II)	39

5.2.2 Impact of wear and tear on photocatalytic ZnO surface coatings (Paper III).....	44
5.3 Photo-induced effects of commercial photocatalytic SaniTise™ and BIOCLEAN®-window glasses (Paper IV)	48
SUMMARY	53
SUMMARY IN ESTONIAN	55
ACKNOWLEDGEMENTS	57
REFERENCES.....	58
PUBLICATIONS	67
CURRICULUM VITAE	134
ELULOOKIRJELDUS.....	136

LIST OF PUBLICATIONS

- I. **Danilian, D.**; Bundrück, F. M.; Kikas, A.; Käämbre, T.; Mändar, H.; Gogos, A.; Kiisk, V.; Link, J.; Stern, R.; Ivask, A.; Kisand, V.; Pärna, R. Reusable magnetic mixture of $\text{CuFe}_2\text{O}_4\text{-Fe}_2\text{O}_3$ and TiO_2 for photocatalytic degradation of pesticides in water. *RSC Advances* **2024**, 14, 12337–12348, <https://doi.org/10.1039/d4ra00094c>.
- II. Rosenberg, M.; Visnapuu, M.; Saal, K.; **Danilian, D.**; Pärna, R.; Ivask, A.; Kisand, V. Preparation and Characterisation of Photocatalytically Active Antibacterial Surfaces Covered with Acrylic Matrix Embedded Nano-ZnO and Nano-ZnO/Ag. *Nanomaterials* **2021**, 11, 3384, <https://doi.org/10.3390/nano11123384>.
- III. Kook, M.; Kaur, H.; **Danilian, D.**; Rosenberg, M.; Kisand, V.; Ivask, A. Durability of Photocatalytic ZnO-Based Surface Coatings and Preservation of Their Antibacterial Effect after Simulated Wear. *J. Coat. Technol. Res.* **2024**, 1–12, <https://doi.org/10.1007/s11998-023-00868-2>.
- IV. Kisand, V.; Visnapuu, M.; Rosenberg, M.; **Danilian, D.**; Vlassov, S.; Kook, M.; Lange, S.; Pärna, R.; Ivask, A. Antimicrobial Activity of Commercial Photocatalytic SaniTise™ Window Glass. *Catalysts* **2022**, 12, 197, <https://doi.org/10.3390/catal12020197>

OTHER PUBLICATIONS THAT ARE NOT INCLUDED IN THE THESIS

- V. Kaur, H.; Rosenberg, M.; Kook, M.; **Danilian, D.**; Kisand, V.; Ivask, A. Antibacterial Activity of Solid Surfaces Is Critically Dependent on Relative Humidity, Inoculum Volume and Organic Soiling. **2023**, <https://doi.org/10.1101/2023.03.28.534510>.
- VI. Kisand, K.; Sarapuu, A.; Danilian, D.; Kikas, A.; Kisand, V.; Rähn, M.; Treshchalov, A.; Käärik, M.; Merisalu, M.; Paiste, P.; et al. Transition Metal-Containing Nitrogen-Doped Nanocarbon Catalysts Derived from 5-Methyl-resorcinol for Anion Exchange Membrane Fuel Cell Application. *J Colloid Interf Sci* **2021**, 584, 263–274, <https://doi.org/10.1016/j.jcis.2020.09.114>.

AUTHOR'S CONTRIBUTION

The list of publications reflects the collaborative effort of several researchers, a necessity due to the complex nature of the material, which demands diverse experimental techniques for characterisation and the expertise of multiple scientists. The results achieved in the research papers are the product of collective work.

Details of the author's contributions to each research paper are outlined below, with Roman numerals corresponding to the publication list.

- I. The Author was responsible for writing the manuscript and combining figures. The Author synthesized materials, measured and analyzed XPS, Raman, and optical absorption spectra and conducted photocatalytic analyses. The Author was responsible for delegating and organising all other characterisation methods.
- II. The Author performed XPS experiments and analysed the data to determine surface elemental composition, conducted hydrophilicity measurements, and contributed to experiments to analyse photocatalytic activity. The Author wrote corresponding methods and results parts.
- III. The Author analyzed surface elemental composition using XPS, conducted hydrophilicity measurements of surfaces and assisted in photocatalytic analysis. He wrote corresponding methods parts and contributed to description of results.
- IV. The Author conducted hydrophilicity measurements, contributed to the writing of the methods and results section.

ABBREVIATIONS AND SYMBOLS

2,4-D	– 2,4-Dichlorophenoxyacetic acid, a type of herbicide
A_{ads}	– Adsorbed acceptor
CB	– Conduction band
D_{ads}	– Adsorbed donor
DRS	– Diffuse reflectance spectroscopy
e^-	– Electron
E_b	– Binding energy
EDX	– Energy dispersive x-ray analysis
E_g	– Band gap
E_k	– Kinetic energy
eV	– Electron volt
h^+	– Hole (electronic vacancy)
h ν	– Photon energy
ICP-OES	– Inductively coupled plasma optical emission spectroscopy
NEXAFS	– Near edge x-ray absorption fine structure
OH^-	– Hydroxyl group
$\bullet\text{O}_2^-$	– Superoxide ion
$\bullet\text{OH}$	– Hydroxyl radical
$\bullet\text{HO}_2$	– Hydroperoxide radical
PPMS	– Physical property measurement system
SD	– Standard deviation
PC	– Photocatalyst
ROS	– Reactive oxygen species
SEM	– Scanning electron microscopy
STEM	– Scanning transmission electron microscopy
SS	– Stainless steel
UHV	– Ultra-high vacuum
UV-Vis	– Ultraviolet-visible spectroscopy
UVA	– Ultraviolet A (315–400 nm wavelength)
VB	– Valence band
XAS	– X-ray absorption spectroscopy
XPS	– X-ray photoelectron spectroscopy
XRD	– X-ray diffraction

1. INTRODUCTION

In recent years, the intersection of photocatalysis and environmental science has given rise to innovative solutions for some of the most pressing ecological and health-related challenges [1, 2]. Due to the relentless pace of industrialization and urbanization, effective and sustainable methods for removing harmful pollutants and killing pathogenic microbes are urgently required. Traditional methods of water treatment and disease prevention often involve the use of chemicals that can further contribute to environmental pollution or are energy-intensive and costly [3, 4]. Among innovations offered by nanotechnology, nanosized photocatalysts have been suggested as promising materials to be used for addressing issues related to water pollution, air purification, and spreading infectious diseases [3–8].

Photocatalytic technology stands out for its ability to harness the energy of light, typically from the sun, to catalyze the breakdown of various organic compounds and microorganisms in an environmentally friendly and cost-effective manner [4, 6, 9, 10]. Photocatalysis is a process that facilitates light-activated materials to initiate or accelerate chemical reactions. Photocatalysts can degrade harmful pollutants and pathogens, offering a sustainable approach to environmental remediation and disinfection [3–8].

The initial focus of photocatalytic research was predominantly on TiO₂-based materials due to their strong oxidative power, stability, and non-toxicity [11]. More recently, a broad range of materials and composites have been investigated in photocatalytic applications. Examples include ZnO, ZnO decorated with Ag nanoparticles, and mixtures of TiO₂ and other oxides including CuFe₂O₄ and Fe₂O₃ [12–14]. The incorporation of silver (Ag) into zinc oxide (ZnO) enhances its photocatalytic and antimicrobial efficacy [15]. Similarly, the combination of TiO₂ with magnetic CuFe₂O₄-Fe₂O₃ particles facilitates the easy recovery and reuse of photocatalysts, marking a significant advancement in making photocatalytic processes more practical and environmentally sustainable [16].

The central theme of this thesis is photoinduced activity of materials, mainly photocatalysis. In the second chapter of this thesis a literature overview on photo-induced processes such as photocatalysis and light-induced hydrophilicity is given. Then literature overview about photocatalytic water treatment and photocatalytic antimicrobial coatings is given. In the last part of this section a closer look at the experimental techniques used in the work is made. In the third chapter the author has outlined the motivation and aims of the thesis. Chapter four covers the information about material synthesis and methods. In chapter five results are discussed in following order: (i) first section of results focus on the free photocatalytic particles used for water purification (**Paper I**) (ii) on the results obtained from investigations of particles in acrylic matrix (**Paper II** and **III**) and (iii) on the photocatalytic activity and wettability of commercial coatings (**Paper IV**).

2. LITERATURE REVIEW

2.1 Photocatalysis

Photocatalysis is a process of acceleration of a light-induced reaction by introduction of a light-absorbing catalyst. Materials which absorb light and as a result act as catalysts are called photocatalysts.

In a heterogeneous photocatalysis, a catalyst (PC) is activated by the absorption of a photon whose energy, $h\nu$, is larger than the band gap (E_g) of the material [17–19]. As a result (Fig. 1), an electron (e^-) is excited to the conduction band (CB) of the photocatalyst and a hole (electronic vacancy, h^+) is created in the valence band (VB) [20, 21]. This process is illustrated in Figure 1. If the lifetimes of e^- and h^+ are sufficiently long, they can diffuse to the surface of the semiconductor and participate in redox reactions. The most important attributes of a photocatalytic material are the positions of the valence band maximum and the conduction band minimum relative to the Fermi level (E_F) [20]. The positions of the band edges determine the oxidizing power of holes, and the reducing power of excited electrons. This determines the oxidizing power of holes and the reducing power of electrons. If photogenerated h^+ near the photocatalyst's surface have enough energy, they can directly oxidize adsorbed pollutants (D_{ads}), or alternatively they can oxidize water molecules or surface hydroxyl groups (OH^-) to form hydroxyl radicals ($\bullet OH$) through the following reactions [19]:

- PC absorbs a photon and generates a pair of e^- and h^+ : $PC + h\nu \rightarrow PC(h^+ + e^-)$
- h^+ oxidizes H_2O or OH^- , leading to the creation of hydroxyl radicals:
 $h^+ + H_2O \rightarrow \bullet OH + H^+ / h^+ + OH^- \rightarrow \bullet OH$
- h^+ interacts with D_{ads} to produce oxidized forms: $h^+ + D_{ads} \rightarrow D_{ads}^+$

In the presence of oxygen, e^- contributes to reducing oxygen to form superoxide ($\bullet O_2^-$) ions. Superoxide anions can undergo further reactions with protons and adsorbed water to yield hydroperoxide radicals ($\bullet HO_2$), forming hydrogen peroxide (H_2O_2). Hydrogen peroxide can react with superoxide to generate additional hydroxyl radicals. These reactions may occur as follows [18, 19]:

- Oxygen is reduced by an e^- to form superoxide: $O_2 + e^- \rightarrow \bullet O_2^-$
- Superoxide anions react with H^+ to produce hydroperoxide radicals:
• $\bullet O_2^- + H^+ \rightarrow \bullet HO_2$
- Hydroperoxide radicals can decompose into oxygen and hydrogen peroxide:
 $2 \bullet HO_2 \rightarrow O_2 + \bullet H_2O_2$
- Hydrogen peroxide and superoxide ions react to produce hydroxyl ions, hydroxide radicals, and oxygen: $H_2O_2 + \bullet O_2^- \rightarrow OH^- + \bullet OH + O_2$

These processes facilitate the formation of highly reactive species such as hydrogen peroxide, superoxide ions, hydroperoxide, and hydroxyl radicals. The latter four are called reactive oxygen species (ROS). With the help of the formed reactive species photocatalytic reactions are able to oxidize various organic pollutants [18, 19]. Therefore, photocatalytic materials can convert pollutants into CO_2 and H_2O under the sunlight.

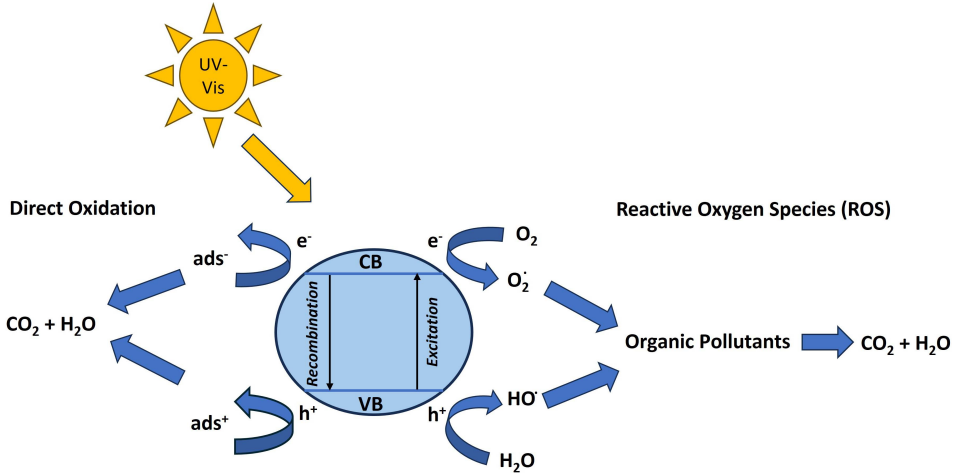


Figure 1. Schematic representation of photocatalytic mechanism. The exposure of photocatalyst to UV-Vis light results in the excitation of e^- from the VB to the CB. This leaves h^+ in the VB. The excited e^- reacts with O_2 molecules to produce O_2^- , while the h^+ reacts with H_2O to form HO^\bullet . Reactive oxygen species (ROS) oxidize organic pollutants, ultimately converting them into CO_2 and H_2O . Direct oxidation processes also occur, where the holes in the VB can directly interact with adsorbed organic pollutants (ads), leading to their degradation.

During the last three decades, it has been found that titania (TiO_2) is a robust and efficient solar light activated photocatalyst [11, 17, 22–24]. However, its activity is limited by its large band gap – 3.2 eV for the rutile polymorph, and 3.0 eV for anatase TiO_2 – which means that it can only absorb a small fraction of the solar radiation that reaches the Earth’s surface. Anatase is the most active photocatalytic phase of TiO_2 among other crystalline allotropes [5, 17, 19, 24]. The superior performance of anatase is due to its surface structure, which results in higher surface adsorption capacity to hydroxyl groups and oxygen than in case of rutile [25]. Anatase also has a lower charge carrier recombination rate than in case of rutile [25].

Nevertheless, there are also factors that limit the photocatalytic efficiency of anatase TiO_2 , including the limited absorption of visible light and the short lifetime of photogenerated electrons. In addition, especially if used in nanoparticle form and in liquid environments (e.g., for water purification), anatase can be difficult to recover from a photocatalytic reactor after its use. [9, 24]. Various methods have been proposed to improve the performance of anatase TiO_2 . For

example, anatase TiO_2 can be combined with rutile TiO_2 , as is done in the commercial Evonik Aeroxide P25 (formerly Degussa P25) photocatalyst. P25 is a flame-made multiphasic TiO_2 nanoparticle powder containing anatase and rutile phases in a ratio of about 3:1. The past decades have witnessed the wide application range of P25. It has become a benchmark material for studying photocatalytic mechanisms, materials, and processes [9].

Other strategies to enhance anatase TiO_2 include band-gap engineering and combination with other semiconductors or metals [19, 26]. Combining anatase with other semiconductors is particularly promising since it is expected to increase photocatalytic performance via extending charge carrier lifetimes [27]. Moreover, it is also possible to modify other properties of anatase-based photocatalysts, e.g. by combining anatase with a magnetic material to produce magnetic composite photocatalyst that can be recovered from solution using powerful magnets [28, 29].

Another well-known photocatalyst is zinc oxide (ZnO) [30]. Like anatase, ZnO is a wide band gap semiconductor – its band gap of 3.3 eV is too large to allow it to absorb visible light, but it has shown high photocatalytic activity under UV radiation. However, ZnO differently from TiO_2 has high electron mobility, which enhances reaction kinetics. ZnO has higher photocatalytic activity under UVA compared to TiO_2 . This has been attributed to its ability to absorb a broader UV spectrum [31]. ZnO is often highlighted for its potential application as antibacterial material, since it releases Zn ions [32, 33].

Similarly to TiO_2 there are different strategies to modify ZnO to shift its band-gap closer to visible light or to enhance its properties for specific applications (for example, antibacterial coatings). For ZnO such modification involves doping, combining it with other semiconductors or metals, or optimizing oxygen vacancies in ZnO [34–36].

2.2 Photocatalyst-driven hydrophilicity

Light-induced hydrophilicity is a property of materials whereby their surfaces become more hydrophilic when exposed to (UV) light [37]. This phenomenon was first discovered in titania films in 1998 [38]. This discovery has motivated extensive research into undoped and doped titania surfaces aimed at developing anti-fogging coatings for clear substrates like glass [39–41].

The underlying process of light-induced hydrophilicity involves the absorption of photons with energy exceeding the semiconductor's band gap, exciting electrons to the CB and leaving holes in the VB. A low recombination rate of electrons and holes is vital, allowing them to migrate to the surface [42, 43]. In the case of TiO_2 , photogenerated electrons convert Ti^{4+} cations to Ti^{3+} , while holes get trapped at lattice sites or near the material surface, weakening the bond between Ti and lattice oxygen. This leads to oxygen liberation, the creation of oxygen vacancies, and subsequently, a more hydroxylated surface due to dissociative water adsorption, as presented in Figure 2. The increased number of hydroxyl (-OH)

groups on the surface enhances van der Waals forces and hydrogen bonding with water molecules, enhancing cohesion between liquid droplet and solid surface. This effect intensifies under prolonged UV light exposure, reducing the contact angle of water droplets to near zero degrees and rendering the surface hydrophilic [39].

Furthermore, light-induced hydrophilicity can coexist with photocatalytic activity, which has enabled the development of self-cleaning windows. This self-cleaning mechanism operates in two stages: the photocatalytic breakdown of organic and inorganic residues followed by the effective removal of these residues, facilitated by the hydrophilic surface that allows for easy washing, even by natural rainfall. This two-step process ensures that windows not only stay clear of pollutants but also remain clean, showcasing the dual benefits of titania's light-activated properties [39, 45].

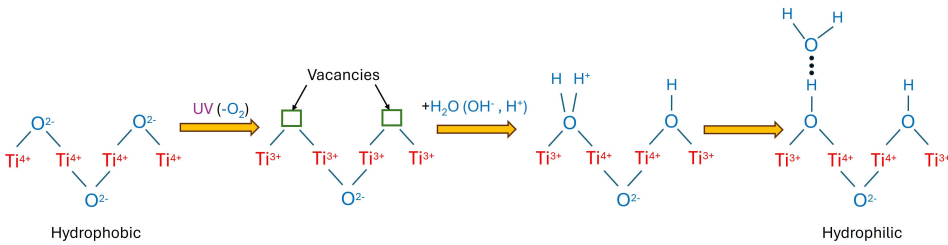


Figure 2. Illustration of photoinduced hydrophilicity: Electrons reduce Ti^{4+} cations to Ti^{3+} , leading to the ejection of oxygen atoms (formation of oxygen vacancies). These vacancies enhance the surface's affinity for water molecules, thereby making the surface hydrophilic.

2.3 Photocatalyst materials in antimicrobial applications

Antimicrobially active materials have recently gained significant attention as they have been suggested to hold great promise in controlling the spread of microbial infections [46]. Most microbial infections spread either through air or via surfaces. As such, air filters and high touch surfaces (\sim surfaces that are frequently touched) are the most evident areas of application for antimicrobial materials [42, 43]. The introduction of antimicrobial surface materials that prevent the adhesion, proliferation or reduce the residence time of microbes would potentially provide great socioeconomic and health benefits [47]. In general, the main types of antimicrobial surfaces are (i) those that act via the release of an antimicrobial agent, (ii) those that act upon direct contact between the microbe and the surface and (iii) structured surfaces that prevent the binding of microbial cells to the surface [48]. The efficacy of antimicrobial coatings in reducing microbial bio-burden has been most clearly demonstrated in laboratory conditions, but it has also been studied in real-life situations. For example, in reference [49] it was shown that the use of copper surfaces [50–52] led to a decrease in the number of hospital-acquired infections. Copper along with silver, belongs to the most

widespread class of antimicrobial surfaces, in which the antibacterial active agent is constantly released from the surface [53]. One of the drawbacks of such surfaces is the accumulation of dead bacterial mass on the surfaces and, subsequent masking of the active surface [54]. This issue could be resolved by surfaces that also eliminate dead bacterial mass. Previous studies of our lab [26, 55, 56] have demonstrated that photocatalytically active TiO₂ surfaces may, in addition to killing bacteria, also lead to the photooxidation of bacterial debris and, thus, the removal of dead bacterial mass from such surfaces. This property can facilitate the extended use of TiO₂-based antimicrobial surfaces [55].

Besides pure photocatalytic materials, an encouraging approach in the context of more effective antimicrobial surfaces is the use of composite materials, which include a combination of different antimicrobial agents and mechanisms of antimicrobial action. The introduction of nano-ZnO/Ag composites has been particularly noteworthy due to their enhanced antimicrobial properties, which combine (i) antimicrobially active Zn and Ag ion release, (ii) direct microbial contact killing, and (iii) enhanced ROS generation facilitated by the photocatalytic charge separation process in ZnO/Ag systems [14], which significantly amplifies ROS production compared to ZnO alone. This amplification results from the effective separation of charge carriers within the composite material, reducing recombination rates and enhancing the photocatalytic reaction under both UV and visible light spectra.

In order to claim antimicrobial activity of a surface, its efficacy has to be proven using a relevant, most often a standard test method [57]. The most widely used standard for testing the antimicrobial efficacy of photocatalytic materials is ISO 27447 method [57], titled “Test Method for Antibacterial Activity of Semiconducting Photocatalytic Materials”, and the most frequently used test bacteria include *Escherichia coli* (*E.coli*), *Staphylococcus aureus* (*S. aureus*), *Pseudomonas aeruginosa* (*P. aeruginosa*), which have considered also medical models [23, 58]. Some of antimicrobial efficacy test methods also get closer to real-life use settings and focus on the residual activity of these materials after repeated use to assess their long-term durability and effectiveness, also after wear and tear [54]. Such assessments are crucial for determining the practical utility of these materials in scenarios where they would be used continuously, such as in hospital settings or public spaces. This activity analysis helps in understanding the life-cycle and potential maintenance requirements of antimicrobial coatings, ensuring they remain effective over time and do not contribute to bacterial resistance.

An important aspect of analyzing the antimicrobial activity of surface-coated materials is understanding the mode of action of these surfaces [59]. The main proposed mode of action of photocatalytic surfaces is the production of ROS and contact killing [60], however depending on material also other mechanisms, such as release of ions can take place [61]. As emphasized in previous studies, it is the synergistic effect of these mechanisms that is essential for enhanced antimicrobial effect of photocatalytic surfaces.

2.4 Photocatalysis-based water treatment

Access to clean and safe drinking water is essential for life. Although the quality of drinking water has remarkably improved compared with the past [62, 63], the increased industrial and agricultural activities pose new threats mainly related with the release of various chemicals. One class of the potential “new” environmental contaminants is pesticides, chemical compounds used in increasing quantities to inhibit the growth or survival of unwanted organisms. Due to their extensive application on soil but also resulting from spills and disposal, pesticides may accumulate in different environmental compartments [64], including surface water or groundwater [65]. Various local drinking water treatment technologies (e.g., ozone, ultraviolet, reverse osmosis) have been recently developed [66, 67], for water cleanup. However, photocatalysis carried out by novel nanotechnological photocatalysts stands out as an alternative and promising approach for water treatment [68–72]. Yet in practical applications, the main drawback of nanoscale photocatalysts is their poor collectability.

To improve the TiO_2 collectability it can be combined with a magnetic material (Fig. 3). One of such materials is ferrimagnetic maghemite ($\gamma\text{-Fe}_2\text{O}_3$) [73], however, it has low stability. The most common form of Fe_2O_3 , hematite ($\alpha\text{-Fe}_2\text{O}_3$) is a stable material with a fairly narrow bandgap (2.2 eV), but with a very weak magnetic moment due to its canted antiferromagnetic order [74]. Besides its weak magnetic properties, hematite has notably rapid recombination of the photo-generated charge carriers, which significantly limits its photocatalytic potential [75, 76]. A promising strongly magnetic material with high magnetic stability near room temperature (Curie temperature as high as $\sim 750\text{K}$) is CuFe_2O_4 [77]. This material could be considered more resistant to photocorrosion or oxidative changes under ambient conditions compared to binary iron oxide-based materials, because it does not contain ferrous iron (such as magnetite) and does not depend on vacancies in structure (like maghemite), both factors typically result in the transformation to a fully oxidized, stable hematite phase in an oxidative environment. CuFe_2O_4 material features a smaller band gap value (~ 1.6 eV) compared to iron oxide materials. However, its photocatalytic effectiveness is constrained by charge recombination, a common issue for materials with strong light absorption and small band gaps. Consequently, based on our current knowledge, there is no material that adequately combines sufficient photocatalytic activity with satisfactory magnetic collectability.

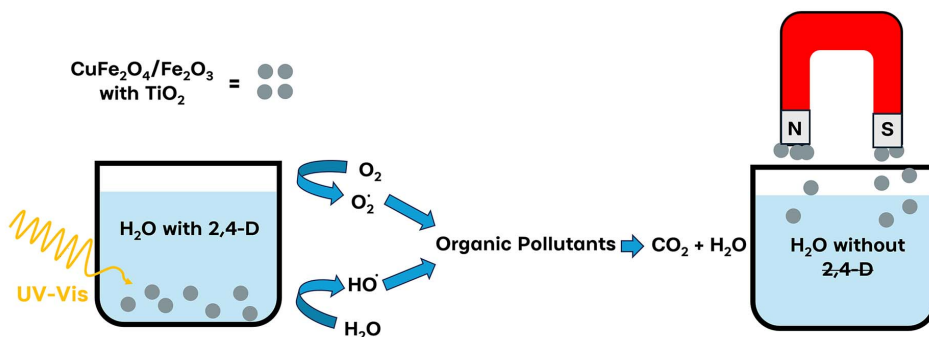


Figure 3. Schematic representation of TiO₂-P25 mixed with magnetic CuFe₂O₄-Fe₂O₃ nanocomposites, demonstrating improving photocatalytic water treatment and enabling easy recovery of the catalyst, with effective degradation of pollutants such as 2,4-D.

At present, photocatalytic degradation of harmful organic pollutants can be realistically applied to small to medium size water purification setups, once sufficient efficiency of the process as well as recyclability of the photocatalyst materials are ensured [9, 78, 79]. An important determinant is also the non-toxicity of the reaction end-products, especially when photocatalytic degradation concerns phenolic pollutants [10].

2.5 Key techniques for the characterisation of photocatalysts

Understanding of the physico-chemical properties of photocatalytic materials is crucial for their development and potential application. This section explains the main methods used to examine these materials in my research. Each technique provides insight into different important features of the photocatalysts, such as their elemental composition, surface structure and performance potential. In this thesis X-ray Photoelectron spectroscopy (XPS), Ultraviolet-Visible (UV-Vis) spectroscopy, X-Ray Diffraction (XRD), and Scanning transmission electron microscopy (STEM) were used to characterize photocatalytic materials. These techniques together have a potential to provide us more detailed understanding of the photocatalysts, helping to improve their performance.

2.5.1 X-ray photoelectron spectroscopy

X-ray photoelectron spectroscopy (XPS) provides detailed information about the elemental composition of a surface and the chemical states of surface atoms, enabling therefore an understanding of the active surface of a photocatalyst. XPS can identify the oxidation states of metals such as copper and titanium, which influence the electronic properties and, consequently, the photocatalytic performance of materials [80]. This information is critical for understanding the photo-

catalyst's activity. For instance, the presence of copper in oxidation states Cu^{1+} and Cu^{2+} can significantly affect a photocatalyst's ability to absorb light and activate chemical processes [81]. Cu^{1+} might be associated with a reduced band-gap, allowing the material to absorb visible light more efficiently than materials with only Cu^{2+} [82]. This capability can extend the operational wavelength range of photocatalysts, enhancing their effectiveness under visible light [6] .

XPS is based on the photoelectric effect. When the sample is exposed to X-rays of a specific photon energy, it results in the emission of photoelectrons from the surface of material. For solid materials, the excited electrons must have sufficient energy to overcome the work function of the surface to be emitted. With known photon energy and the solid's work function, the binding energy of electrons within the sample can be calculated using the equation [83]:

$$E_b = h\nu - E_k - \Phi \quad (1.1)$$

The photoelectron spectrum depicts the number of emitted electrons as a function of their kinetic energy.

XPS is a surface sensitive technique. This sensitivity stems from the electrons' limited mean free path in materials. Typically, for soft X-rays (photon energy $< 2 \text{ keV}$), this path is under 2 nm for the majority of elements, highlighting the technique's surface sensitivity [83–85].

The utility of XPS extends to identifying elements in the surface region due to the unique binding energies of core electrons of different elements. It also excels in assessing the chemical states of surface atoms. For instance, the formation of an oxide from a metal involves the transfer of electron density from the metal atoms to the oxygen atoms, due to oxygen's higher electronegativity. This transfer leaves the metal atom with a partial positive charge, and as a result, more work is required to remove an additional electron from the metal atom. In other words, the core electron binding energies of the metal atom are higher in the oxide than in the elemental metal – this is known as a chemical shift. Besides photoelectron peaks, photoelectron spectra can also display structures attributed to Auger electrons, as well as shake-up and shake-off satellites and multiplet splitting. Auger electron emission is an internal atomic process unaffected by the photon energy, contrasting with the variable kinetic energy of photoelectrons. Shake-up satellites occur when an ejected photoelectron excites a valence electron to a higher level, reducing the core electron's energy and forming satellites in the spectra. Similarly, shake-off satellites result from the complete ejection of a valence electron. Multiplet splitting, observed in materials with unpaired valence electrons, arises from the interaction between an unpaired electron in the core and an outer shell, leading to a multippeak structure in the spectra.

2.5.2 Ultraviolet-visible spectroscopy

Ultraviolet-visible spectroscopy (UV-Vis) is a fundamental tool for characterizing photocatalysts. It allows for determining width of the photocatalyst's band gap, which is a crucial parameter characterizing its light absorption properties and therefore, the conditions for its photocatalytic activity [86].

UV-Vis spectroscopy is a widely utilized analytical technique to characterize the absorption of ultraviolet or visible light by a substance. The principle underlying UV-Vis spectroscopy is based on the fact that visible or ultraviolet photon has enough energy to promote electron excitation from an occupied state to an unoccupied state

The basic equation governing UV-Vis absorbance, according to the Beer-Lambert Law, is [87]:

$$A = \epsilon lc \quad (1.2)$$

Where A is the absorbance (a unitless measure), ϵ is the molar absorptivity coefficient ($\text{L mol}^{-1}\text{cm}^{-1}$), l is the path length of the sample cell (cm), and c is the concentration of the absorbing species (mol L^{-1}). This equation illustrates that absorbance is directly proportional to the concentration of the absorbing species in the solution and the path length through which the light passes.

As a particular case of UV-Vis measurement, Diffuse reflectance spectroscopy (DRS) is employed to measure the diffuse reflectance of a sample. DRS is particularly useful for analyzing powdered materials that cannot be dissolved in any solvent for traditional UV-Vis spectroscopy. This technique involves directing light onto a sample and measuring the light scattered back from the surface. The obtained spectrum is then converted to an equivalent absorption spectrum using the Kubelka-Munk function [86]:

$$F(R) = \frac{(1-R)^2}{2R} \quad (1.3)$$

Where $F(R)$ – is the Kubelka-Munk function and R – is the reflectance of the material. Kubelka-Munk function is crucial for understanding the optical properties of materials like semiconductors.

UV-Vis spectroscopy is pivotal for quantitative analysis in various chemical, physical, and biological research areas. It enables the determination of the concentration of solutes in solution, characterizing the absorption spectrum of compounds, which can reveal structural information, and monitoring the progress of chemical reactions. The technique's versatility extends to studying molecular orbitals, bonds, and the electronic structure of compounds.

The spectral range of UV-Vis spectroscopy is typically from about 200 nm (deep UV) to 800 nm (into the visible spectrum), covering the absorbance region of most organic compounds and many inorganic compounds [88]. The method's simplicity, non-destructive nature, and minimal preparation required for samples make UV-Vis spectroscopy a fundamental tool for scientists in diverse fields

ranging from chemistry and biochemistry to environmental science and pharmacology. It is especially crucial for analyzing compounds like pigments, dyes, and biomolecules such as proteins and nucleic acids, providing insights into their concentration levels and structural properties.

2.5.3 X-ray diffraction

X-ray diffraction (XRD) is a technique for characterizing the crystal structure of photocatalysts. Understanding the crystal phase and orientation of a material is crucial for optimizing its photocatalytic performance, as these factors can significantly influence light absorption, charge carrier transport, and surface reactivity.

XRD is a powerful analytical technique based on the diffraction of X-rays by the crystalline structures within a material. When a crystalline sample is illuminated with X-rays of a specific wavelength, the rays are scattered in various directions. According to Bragg's Law, constructive interference of these scattered X-rays occurs at specific angles, depending on the distance between the planes in the crystal lattice and the incident X-ray wavelength. This principle is encapsulated in the equation [89]:

$$n\lambda = 2d \sin \theta \quad (1.4)$$

where n is an integer (the order of diffraction), λ is the wavelength of the incident X-ray, d is the distance between the crystal planes, and θ is the angle of incidence. The resulting diffraction pattern, which includes peaks at angles where constructive interference occurs, provides a unique "fingerprint" of the material's crystalline structure [87].

XRD is instrumental in identifying the phase composition of materials, elucidating crystal structures, and determining lattice parameters. Its ability to detect and quantify phases within a mixture, assess material purity, and measure the size of crystalline domains makes it indispensable in materials science. The technique's sensitivity to structural arrangement means it can distinguish between different polymorphs of a substance, each of which may exhibit distinct physical and chemical properties.

2.5.4 Scanning transmission electron microscopy

Scanning transmission electron microscopy (STEM) is a powerful, high-resolution imaging technique that plays a vital role in nanomaterials research in general. It enables the visualization of a nanomaterials morphology, composition, and elemental distribution at the atomic level. When applied on photocatalytic materials, such information is invaluable for understanding the structure-function relationship in photocatalysts and for designing photocatalytic materials with improved functionalities.

STEM combines scanning electron microscopy (SEM) principles and traditional Transmission electron microscopy (TEM) to provide detailed images at the

atomic or molecular level. In STEM, a focused beam of electrons is scanned in a raster pattern over a thin specimen. As electrons interact with the sample, they can be scattered elastically or inelastically, with detectors positioned to capture various signals generated from these interactions, including transmitted electrons, secondary electrons, and X-rays [88].

The high-resolution images produced by STEM result from the electron beam's reduced wavelength compared to visible light, allowing for the examination of structures on the nanoscale. Additionally, STEM can be equipped with various analytical tools, such as Energy-dispersive X-ray spectroscopy (EDX) for chemical analysis and Electron energy loss spectroscopy (EELS) for investigating the electronic structure of materials.

STEM is particularly valued for its ability to provide high-resolution structural information and compositional and electronic information about the sample [89]. This makes it a versatile tool in materials science for studying the morphology, crystallography, and chemical composition of materials at the nanometer or even atomic scale. The technique's depth of information makes it crucial for the advancement in nanotechnology, semiconductor research, and the development of advanced materials.

3. MOTIVATION AND AIM OF THE WORK

This thesis is dedicated to advance photocatalytic materials for water treatment and antimicrobial applications, particularly emphasizing their synthesis, characterisation, and efficacy testing. The overarching goal behind the activity is to contribute to development of efficient, collectable and reusable water treatment photocatalyst and enhancement of photocatalytic antimicrobial coatings.

The specific aims were:

- **To synthesize photocatalytic materials for water treatment and antimicrobial applications, specifically:**
 - Collectable and reusable novel photocatalyst based on mixture of TiO₂-P25 combined with magnetic CuFe₂O₄-Fe₂O₃.
 - Real-life applicable novel photocatalytic ZnO-based surface coatings.
- **To relate photocatalytic efficiency of physico-chemical properties of photocatalytic materials, specifically to clarify:**
 - Changes in crystal structure, composition, particle size, elemental distribution, surface chemical species and UV-Vis absorption of novel photocatalyst based on mixture of TiO₂-P25 combined with magnetic CuFe₂O₄-Fe₂O₃. Before and after magnetic separation, collection and photocatalytic reuse.
 - Distribution of nano-ZnO in acrylic matrix.
 - Surface chemical species of SaniTise™ and BIOCLEAN®.
- **To clarify the relationship between photocatalytic efficiency and light induced surface wettability, specifically in case of:**
 - Novel photocatalytic ZnO-based surface coatings for antimicrobial applications on plywood and stainless-steel.
 - Commercial glass surfaces SaniTise™ and BIOCLEAN®.
- **To assess the efficiency of photocatalytic materials, specifically:**
 - Mixture of TiO₂-P25 combined with magnetic CuFe₂O₄-Fe₂O₃ before and after magnetic collection for photocatalytic water purification from 2,4-D, as hardly degradable model pollutant.
 - ZnO-based surface coatings for photocatalytic antimicrobial application.
 - Clarify the photocatalytic efficiency of commercial glass surfaces SaniTise™ and BIOCLEAN®. Results provided information about photocatalytic efficiency of commercially available products, and this helped to evaluate efficiency of prepared coatings.

- **To clarify the impact of wear and tear on photocatalytic activity and wettability of coatings, specifically:**
 - Synthesized nano-ZnO-based acrylic coatings and commercial microsized ZnO-based coating on stainless steel.
- **To propose strategies for developing novel photocatalytic materials and coatings with enhanced performance, specifically exploring:**
 - Magnetic collectability and reusability of mixture of TiO₂-P25 combined with magnetic CuFe₂O₄-Fe₂O₃.
 - ZnO-based acrylic coatings on wood and stainless steel for antimicrobial applications.

The statements presented for defense in this thesis are:

- Novel magnetically collectable and reusable photocatalyst can be developed by combining TiO₂-P25 with CuFe₂O₄-Fe₂O₃ for water treatment.
- Novel photocatalytic surface coatings for antimicrobial applications can be designed from nano-ZnO particles in acrylic matrix.
- Photocatalytic efficiency of ZnO-based acrylic surface coatings can be preserved after simulated wear and tear.
- Surface wettability in case of ZnO on acrylic matrixes are not affected after wear and tear.

The course of this research involves:

- Synthesise novel photocatalytic and magnetically recoverable mixture of TiO₂-P25 with CuFe₂O₄-Fe₂O₃.
- Prepare novel photocatalytic ZnO-based surface coatings.
- Characterise TiO₂-P25 combined with magnetic CuFe₂O₄-Fe₂O₃, ZnO-based surface coatings and commercial glass surfaces (SaniTise™ and BIOCLEAN®).
- Perform investigations of photocatalytic efficiency of TiO₂-P25 combined with magnetic CuFe₂O₄-Fe₂O₃ for 2,4-D degradation in water,
- Perform investigations of photocatalytic efficiency of ZnO-based surface coatings and commercial glass surfaces (SaniTise™ and BIOCLEAN®) for methylene blue degradation on surface.
- Elucidate the impact of wear and tear on photocatalytic activity of nano-ZnO-based acrylic coatings and commercial microsized ZnO-based coating on stainless steel.
- Clarify the relationship between photocatalytic efficiency and light induced surface wettability of ZnO-based surface coatings and commercial glass surfaces SaniTise™ and BIOCLEAN®.

- Analyze data from these experiments to identify the key factors that influence the performance of those materials and use this information in the design of enhanced photocatalysts.

Through these aims, the thesis endeavours to deepen the understanding of photocatalytic materials and their potential for water treatment and antimicrobial applications.

4. MATERIALS AND METHODS

4.1 Photocatalyst synthesis

4.1.1 The synthesis of TiO₂ with CuFe₂O₄-Fe₂O₃

In **Paper I** TiO₂ (Evonik Aeroxide P25, formerly Degussa P25) and precursor reagents Cu(NO₃)₂ × 3H₂O (99% purity, trace metals based), Fe(NO₃)₃ × 9H₂O (99% purity, trace metals based) and NH₄OH (98% purity) were all obtained from Sigma Aldrich. CuFe₂O₄-Fe₂O₃ was synthesized using a co-precipitation method with copper and iron nitrate salts dissolved in deionized water, then precipitated by adding NH₄OH until pH 11 was reached. The precipitate was washed, centrifuged, dried at 60 °C and annealed at 700 °C for 4h. For the photocatalyst TCF-M-5c (see naming convention at Table 1), this oxide powder was mixed with TiO₂ (Evonik Aeroxide P25) in a ratio of 20:80 and annealed at 600 °C for 24 h. The mixture was subjected to magnetic separation to isolate the magnetic fraction (TCF-M) from non-magnetic particles (TCF-NM), adjusting the component ratios. Reference materials used included unmodified TiO₂-P25 and a batch annealed at 600 °C to study the effects of thermal treatment.

Table 1. Materials naming conventions. Table reprinted by CC BY-NC 3.0 Deed licence from **Paper I**.

Codes of material	Description
TiO ₂ -P25	TiO ₂ (Evonik Aeroxide P25)
TiO ₂ -P25 @ 600 °C	TiO ₂ (Evonik Aeroxide P25) annealed at 600 °C for 24 h
CuFe ₂ O ₄ -Fe ₂ O ₃	synthesised CuFe ₂ O ₄ -Fe ₂ O ₃
TCF20-S	20% of the annealed CuFe ₂ O ₄ -Fe ₂ O ₃ powder with 80% of TiO ₂ -P25
TCF-NM	non-magnetic fraction of TCF20-S after magnetic extraction
TCF-M	magnetically extracted fraction of TCF20-S material
TCF-M-5c	TCF-M after 5 cycles of photocatalytic degradation

4.1.2 Synthesis of nano-ZnO and nano-ZnO/Ag

For photocatalytic material from **Paper II** and **Paper III**, the stock solution of Zn(CH₃COO)₂ × 2H₂O (puriss. p.a. Sigma Aldrich) in methanol (27 wt.%) was prepared by stirring and heating under reflux. KOH (22 wt.% Lach-Ner, reagent grade) in methanol was added to the stock solution under continuous stirring, and the mixture was then heated under reflux and stirring in an 80 °C oil bath for 72 h. The suspension was allowed to cool to room temperature, and the resulting white solid was washed with methanol. Nano-ZnO were stored as a methanol containing paste in the dark at room temperature. Nano-ZnO concentration in the paste was determined by thermogravimetric analysis. Silver 2-ethylhexanoate was prepared by mixing together equal volumes of 0.1 M AgNO₃ and 0.1 M sodium

2-ethylhexanoate aqueous solutions. The resulting white precipitate was washed with deionized water and methanol and subsequently left to dry in the dark at room temperature for a week. To produce nano-Zn/Ag composite, nano-ZnO, formed as a nanorods, approximately 20 nm in diameter and 120 nm in length was deposited with Ag using UVA-induced photodeposition to prepare nano-ZnO/Ag composite particles.

4.2 Surface and coating preparation

4.2.1 Nano-ZnO and nano-ZnO/Ag in acrylic matrix on plywood

Squares of plywood (birch, 4 mm thick, 25 × 25 mm) were used as a surfaces to be covered with acrylic-embedded nano-ZnO and nano-ZnO/Ag according procedure described in section 4.1.2. Acrylic clear matt commercial two-component topcoat meant for wooden surfaces (topcoat TZ9310/00 and hardener TH0790/00, Sayerlack, Pianoro, Italy) was used as the acrylic matrix to embed the prepared nano-ZnO and nano-ZnO/Ag particles.

Before applying the nanomaterial-enhanced acrylic matrix material, the wooden surfaces were undercoated (TU0141/00, Sayerlack, Pianoro, Italy) and allowed to dry under ambient laboratory conditions for one week. The nano-ZnO and nano-ZnO/Ag enhanced topcoats were then uniformly brushed onto the surfaces, employing a brushing method to reflect a practical real-world application technique. As a result, the thickness of the coating was determined solely by the method of application and was not specifically tailored. After coating, the surfaces were left to dry at room temperature for another week before further analysis. Wooden surfaces treated with only undercoat and topcoat served as negative controls.

For “nanomaterial controls” in photocatalytic experiments, glass surfaces with (matrix-free) nano-ZnO and nano-ZnO/Ag particles were used. For this, nano-ZnO and nano-ZnO/Ag suspensions were spin-coated onto 25 × 25 mm square cover glasses (2855-25, Corning Inc., Corning, NY, USA). The surfaces were subsequently heated at 200 °C for 6 h to improve nanoparticle adherence to the glass substrates and ensure the removal of organic residues.

4.2.2 ZnO in acrylic matrix on stainless steel

Stainless steel (SS) disks in **Paper III** were used as substrates for the ZnO-based coatings. The disks were thoroughly cleaned with a series of washing steps involving water, acetone, and ethanol, followed by ultrasonic cleaning and air drying. Two types of ZnO were employed for the coatings: commercial micro-sized ZnO (colour pigment Sennelier Zinc White) and in-house synthesized ZnO nanorods (described in 4.1.2). The nano-ZnO particles were incorporated into a two-component acrylic polymer matrix designed for metal surfaces, consisting of a matte topcoat, a hardener, and a thinner (SIRCA S.p.A, Italy). The mixture preparation involved blending the topcoat and hardener, then adding the thinner alone or

mixed with nano-ZnO and commercial micro-ZnO. Nano-ZnO particles were first dispersed in the thinner using an ultrasonic homogenizer and then mixed into the topcoat mixture. The prepared mixtures were applied to the SS disks using a spin coater at 300 rpm for 3 seconds, followed by drying at room temperature for 24 h. This method facilitated the creation of different surface types: a matrix-only surface, a surface with commercial ZnO, and a surface with synthesized ZnO nanorods.

For AISI304L SS disks (Outokumpu, Finland, 8% Ni, 18% Cr, 75% Fe, 2B surface finish), methanol (Sigma-Aldrich, puriss, $\geq 99.8\%$), 1-butanol (Sigma-Aldrich, puriss, $\geq 99.5\%$), KOH (LACH-NER, 90.0%), and $\text{Zn}(\text{CH}_3\text{CO}_2)_2$ (Sigma-Aldrich, $\geq 99.0\%$). All other chemicals were of analytical grade.

Three different treatments were performed to evaluate the durability of nano-ZnO and microstructures-based surface coatings after simulated wear. Two of those dry (D) and wet rubbing (W) methods followed EPA Interim Guidance for Evaluating the Efficacy of Antimicrobial Surface Coatings [90]. The third treatment was based on sandpaper abrasion (A) protocol that is a common method used to test mechanical properties of surfaces and has generally been expected to remove the topmost layer of coatings [91]. A custom automated abrasion tester based on open-source RepRap hardware and software [92] was used for all treatments. D, W, and A treatments were performed for every surface coating type, M, ZnO(c), and ZnO(s), presented in Table 2.

Table 2. Description of surface coatings used in the **Paper III**. Table reprinted following CC BY 4.0 Deed, from **Paper III**.

Surface	Description of coating	Treatment
M	SS (stainless steel) surface coated with acrylic topcoat matrix	No treatment
M_D		Dry rubbing
M_W		Wet rubbing
M_A		Abrasive treatment
ZnO(c)	SS surface coated with commercial ZnO pigment microstructures in acrylic topcoat matrix.	No treatment
ZnO(c)_D		Dry rubbing
ZnO(c)_W		Wet rubbing
ZnO(c)_A		Abrasive treatment
ZnO(s)	SS surface coated with in-house synthesized nano-ZnO in acrylic topcoat matrix.	No treatment
ZnO(s)_D		Dry rubbing
ZnO(s)_W		Wet rubbing
ZnO(s)_A		Abrasive treatment

4.2.3 Commercially available glass Pilkington SaniTise™ and BIOCLEAR®

In **Paper IV** three types of 25 × 25 mm glass surfaces – 4 mm thick Pilkington SaniTise™ glass, which has pyrolytical TiO₂ coating (NipponSheet Glass Co Ltd., Minato City, Tokyo, Japan), 6 mm thick BIOCLEAR® (Saint-Gobain, Courbevoie, France) glass that has TiO₂ anatase coating along with 4 mm thick PLANI-CLEAR® (control glass, Pilkington) were used. According to information from producers, the thickness of the TiO₂ layer on such covered commercial glasses is typically small and in the range of ~15–20 nm [93]

4.3 Characterisation of photocatalytic materials and surfaces

4.3.1 X-ray photoelectron spectroscopy

XPS measurements were conducted using an electron energy analyser (SCIENTA SES 100) and a non-monochromatic twin anode X-ray tube (Thermo XR3E2). The X-ray tube had characteristic energies of 1253.6 eV (Mg K α 1,2 FWHM 0.68 eV) and 1486.6 eV (Al K α 1,2 FWHM 0.83 eV). All measurements took place in Ultra-High Vacuum (UHV) conditions with a pressure of less than 5×10^{-9} mbar. The angle between the analyser and the X-ray source was 45°.

Ar⁺ ion sputtering was performed in UHV conditions at 10^{-8} mbar. The duration of the Ar⁺ beam exposure was 15 min and the Ar⁺ current was 10 mA.

The binding energy scales for the XPS experiments were referenced to the binding energy of the C 1s photoemission line, 284.8 eV. Raw data obtained from the experiments were processed using Casa XPS version 2.3.23 [94]. Data processing steps involved the removal of K α and K β satellites, as well as fitting the components. The Shirley background was used, and a Gauss-Lorentz hybrid function (GL70, Gauss 30%, Lorentz 70%) was employed to fit the components and ensure the best fit.

In **Paper II**, nano-ZnO and nano-ZnO/Ag-covered plywood surfaces were first degassed in a vacuum until the base pressure 1×10^{-8} mbar was reached, then heated twice to 60 °C for 1 hour. Samples in **Paper I** and **IV** were measured without pretreatment.

4.3.2 Scanning transmission electron microscopy with energy-dispersive X-ray spectroscopy

The synthesised materials were characterised in **Paper I** and **Paper II** by STEM-EDX analysis to gain information on the microstructural features and elemental distribution. Materials were prepared by mixing a spatula tip of the respective dry powder with 300 μ L ethanol (> 99.9%, LiChrosolve, Supelco). The material was then sonicated for 2 min and left to sediment for 1 min. 10 μ L from the super-

nant was then drawn through a holey carbon nickel grid. After drying, most of the materials were analysed on a Talos F200X STEM (Thermo Fisher Scientific) and by Titan Themis 200 (FEI) STEM equipped with the SuperX EDX system, both operated at an accelerating voltage of 200 kV. High-Angle Annular Dark-Field (HAADF) STEM images were obtained with EDX elemental maps. Data was processed using the software Velox (Version 3.0.0.815, Thermo Fisher Scientific).

4.3.3 UV-Vis absorbance

Material absorbance measurements in **Paper I** were determined by measuring diffused reflectance using a UV-Visible spectrophotometer equipped with a tungsten lamp and a photomultiplier (Agilent Cary 5000 UV-Vis-NIR, USA). The powdered material was measured in a powder cell (22 mm diameter quartz window with a maximum volume of 1 cm³). Polytetrafluoroethylene (PTFE) signal was used as a baseline for diffuse reflectance spectroscopy, and spectral resolution was 0.1 nm. Measured diffuse reflectance spectra are transformed into the absorption spectra using an equation $A = 2 + \log(1/R)$, where A is absorbance, R is the reflectance of material [95] and 2 is the normalization coefficient.

4.3.4 Contact angle measurements of surfaces

The sessile drop method was used in **Paper II, III and IV** to measure water drop contact angles using a moving platform based on Thorlab DT12 (Newton, NJ, USA) dovetail translation stage [96]. A 2 μ L drop of deionized water was pipetted onto each coated surface. After 10 s, the water droplet was photographed with a Canon EOS 650d camera (Ota City, Tokyo, Japan) using an MP-E 65 mm f/2.8 1–5 \times Macro focus lens. Image analysis software (ImageJ 1.8.0 172; NIH, Madison, WI, USA) for Windows (plugin for contact angle measurement) was used to determine the contact angle formed by the liquid drop on the glass surface [97]. All samples were measured in four replicates. Samples with a contact angle $< 90^\circ$ were considered hydrophilic, and samples with a contact angle $> 90^\circ$ were considered hydrophobic [98].

4.3.5 Other characterisation techniques

XRD. X-ray Diffraction (XRD) patterns in **Paper I** were recorded on diffractometer SmartLabTM (Rigaku, Japan) implementing Bragg-Brentano optical geometry and CuK α radiation (wavelength 0.154178 nm) from rotating anode working at 8.1 kW (45 kV and 180 mA). Powder diffraction database PDF-2 (version 2023) was used for qualitative analysis of phases. Rietveld analysis (program TOPAS 6) was used for a rough estimation of concentrations of the phases.

Raman spectroscopy. Raman spectra of the materials in **Paper I** and **IV** were acquired by using a Raman microscope (inVia, Renishaw, UK) at ambient temperature. The powders were deposited onto a silicon wafer, 514.5 nm emission argon-ion laser was used for excitation and 50x objective was used to focus the laser beam and collect the backscattered light. The incident power was typically kept at 1 mW along with a slight defocusing of the beam (spot size $\sim 10 \mu\text{m}$) to avoid any photoinduced damage to the sample. The spectral resolution of the Raman microscope was approximately 2 cm^{-1} .

ICP-OES. Elemental contents of the materials were quantitatively assessed in **Paper I** by using Inductively Coupled Plasma Optical Emission Spectroscopy (ICP-OES). To this end, $\approx 10 \text{ mg}$ of dry powder was mixed with 3 ml HNO_3 (69%), 1 ml H_2O_2 (30%), and 1 ml HF (40%) and digested using a pressurised microwave (Ultraclave, MLS GmbH, Germany) at $240 \text{ }^\circ\text{C}$ and 100 bar for 10 min. After the digestion process, the mixture was brought till 50 ml using ultrapure water and analysed using Agilent 5110 ICP-OES. The elements were quantified using external calibration with the respective certified aqueous standards (Inorganic ventures).

NEXAFS. Near Edge X-ray Absorption Fine Structure (NEXAFS) measurements in **Paper I** were conducted at the solid-state endstation of the FinEstBeaMS of MAX-IV synchrotron [99, 100]. The NEXAFS measurements were performed in the total electron yield mode by monitoring the sample drain current using ALBA electrometer [99]. The sample current signal was normalised to the incoming flux (simultaneously) measured using the photocurrent signal from a clean gold mesh positioned between the material and the last optical element of the beamline.

Magnetic characterisation. Magnetic properties of the materials in **Paper I** were measured with Physical Property Measurement System (PPMS 14 T, Quantum Design, USA). These properties measured include saturation magnetisation, coercivity, and the critical temperatures. Measurements at and below room temperature were conducted with the Vibrating Sample Magnetometer (VSM) option and the powdered materials were enclosed in appropriate nonmagnetic plastic capsules. High temperature measurements were performed with the VSM OVEN option and materials were attached to the OVEN measurement stick mixed in a drop of recommended Zircar cement. High temperature measurements were scaled to low temperature measurements at the overlapping temperature of 300 K. Magnetic field up to 20 k Oe (2 T) was used to record the hysteresis in magnetic isotherms. Magnetic flux trapping in PPMS superconducting solenoid is accounted for and reported magnetic field is corrected using a Pd standard following the recommended procedure [101]. A small magnetic field of 100 Oe (0.01T) was applied during temperature dependent measurements and magnetic transition temperatures were determined from the extrema in temperature derivative dM/dT .

4.4 Photocatalytic analysis of surfaces

In the comparative study of photocatalytic activity, a similar method was used across **Papers II–IV**, utilizing the degradation of methylene blue (MB) dye to assess the efficacy of the photocatalysts.

The coated surfaces were placed into wells of 6-well microplates, aqueous solution of MB (concentration 10^{-5} M) was pipetted into each well, and the whole plate was covered with UV transparent borosilicate glass to suppress evaporation. Into each well, magnetic stirring bar (7×2 mm) was placed and stirring at 150 rpm was carried out during the whole experiment. To decrease drying effects, all photocatalytic experiments were performed in a preconditioned climatic chamber (Memmert CTC 256, Germany) at 23 °C and 90% relative humidity. Before experiments, the samples with dye solution were preconditioned for 20 min in dark to establish the adsorption equilibrium of MB. After each time interval of the degradation experiment, the MB solution was poured into a standard PS 10-mm optical length cuvette to measure the UV–Vis absorbance of MB using a spectrophotometer (Agilent Cary UV–Vis-NIR 5000, Agilent, USA). The absorbance intensity at 663 nm (characteristic absorbance peak for MB) after the test was compared to the initial intensity to evaluate the degradation of MB. A self-built lamp consisting of 4 fluorescent Hg light bulbs (15 W iSOLde Cleo, $\lambda_{\max} = 355$ nm) was used and the light intensity at test surface height was 2.8–3.2 W/m² at 315–400 nm spectral range (measured using Delta Ohm UVA probe).

4.5 Photocatalytic degradation of pesticide 2,4-D

For **Paper I**, the photocatalytic activity of the materials was evaluated through degradation of 10^{-4} M solution of 2,4-D (PESTANAL, Sigma Aldrich, purity $\geq 98.0\%$) in deionized water. The selected concentration of 2,4-D was above environmental levels, but it was chosen to ensure detectable photocatalytic degradation kinetics. Degradation of 2,4-D was measured during 18 h illumination under a UVA lamp (see description in section 4.4). The presence of 2,4-D was measured as absorbance at 200–400 nm using UV-Vis spectrometer. For photocatalytic experiments, 2,4-D solution with 1 ml⁻¹ of test material was placed to quartz cuvettes, pre-incubated for 30 min at 22.5 °C in climate chamber in the dark and then exposed to UVA light or in the dark. Decay of 2,4-D at 229 nm was measured every 30 min during 18 h UVA irradiation or incubation in the dark.

For repeated use of magnetic photocatalytic materials, the material was reclaimed after a UVA exposure cycle using a magnet that attracted the material to a borosilicate glass barrier. This recovered material was then thoroughly rinsed five times with deionised water and dried in an oven at 70 °C for 12 h.

5. RESULTS AND DISCUSSION

Photocatalysis is based on chemical transformations due to the absorption and utilisation of light energy. Photocatalysts can be prepared in various forms, for example, as free particles, as particles embedded into matrices to form coatings, or as coatings that can be directly deposited onto substrates. The first section of results focuses on free photocatalytic particles (**Paper I**). Then results obtained from investigations of particles in acrylic matrixes are shown (**Paper II and III**). In the last section photocatalytic activity and wettability of commercial coatings are evaluated (**Paper IV**).

5.1 Reusable magnetic photocatalyst for water purification (Paper I)

Photocatalytic water purification has emerged as promising alternative technology to clean drinking water from contaminants [65]. In this research titania has gained attention as the most important photocatalyst [17, 19]. However, TiO_2 efficiency suffers due to the limited visible light absorption of and the short lifetime of photogenerated electrons [24]. In addition, especially nanosized TiO_2 is complicated to remove from photocatalytic reactor after water purification [7, 24].

Various methods have been proposed to improve the performance of TiO_2 [18, 19, 27]. Where one promising approach is to combine TiO_2 , two phases with different bandgaps (rutile and anatase) [25]. This has resulted creation of commercial Evonik Aeroxide P25, where ratio of anatase and rutile is about 3:1 [102]. Other approach is to combine TiO_2 with other semiconductors [24, 27]. One of such semiconductors is Fe_2O_3 in the form of hematite or maghemite [72, 73]. It has been shown that combining $\alpha\text{-Fe}_2\text{O}_3$ and TiO_2 can enhance visible light photocatalytic activity and increase the lifetime of charge carriers [72, 73].

Nevertheless, issue remains related to collectability of TiO_2 . This can be enhanced by introducing magnetic properties to TiO_2 . Previously CuFe_2O_4 has been used to add magnetic properties to photocatalytic TiO_2 [103]. In this thesis a magnetically collectable photocatalyst was developed by synthesizing mixture of $\text{CuFe}_2\text{O}_4\text{-Fe}_2\text{O}_3$ and $\text{TiO}_2\text{-P25}$. The characterisation, photocatalytic activity, and reusability of the $\text{TiO}_2\text{-P25}$ and $\text{CuFe}_2\text{O}_4\text{-Fe}_2\text{O}_3$ mixture is the primary object of the present chapter.

Characteristics of materials

Particle morphologies were measured with STEM. According to STEM $\text{TiO}_2\text{-P25 @ 600 }^\circ\text{C}$ (sample names are given in Table 1) particles agglomerated (particle sizes was around ≈ 200 nm down to tens of nm) and exhibited polydispersity (Fig. 4). $\text{CuFe}_2\text{O}_4\text{-Fe}_2\text{O}_3$ on the other hand had large grain sizes (around 1 μm

down to ≈ 100 nm) (Fig.4). However, the mixed materials TCF20-S, TCF-NM and TCF-M had similar grain size and morphology with respect to the TiO_2 -P25 @ 600 °C.

STEM-HAADF (Fig 4) was used to investigate the distribution of elements. HAADF results indicated the presence of all elements expected from the material's composition. Copper was homogeneously distributed in most of the materials, whereas Fe was distributed in nanoscopic clusters of a few nm in size. After magnetic extraction, in the residual TCF-NM Fe and Cu were barely detectable. This suggests successful magnetic removal of Fe-rich material from TCF20-S. The TCF-M (extracted magnetic fraction) appeared slightly richer in Fe content as well as in nanoscopic Fe clusters throughout the material, while the distribution of Cu was uniform. The presence of Fe and Cu was also seen in the recycled material TCF-M-5c (see Fig 4). It should be noted that TCF-M-5c as measured with other STEM and signal collection time was shorter. This has impacted the intensity of Fe and Cu characteristic fluorescence.

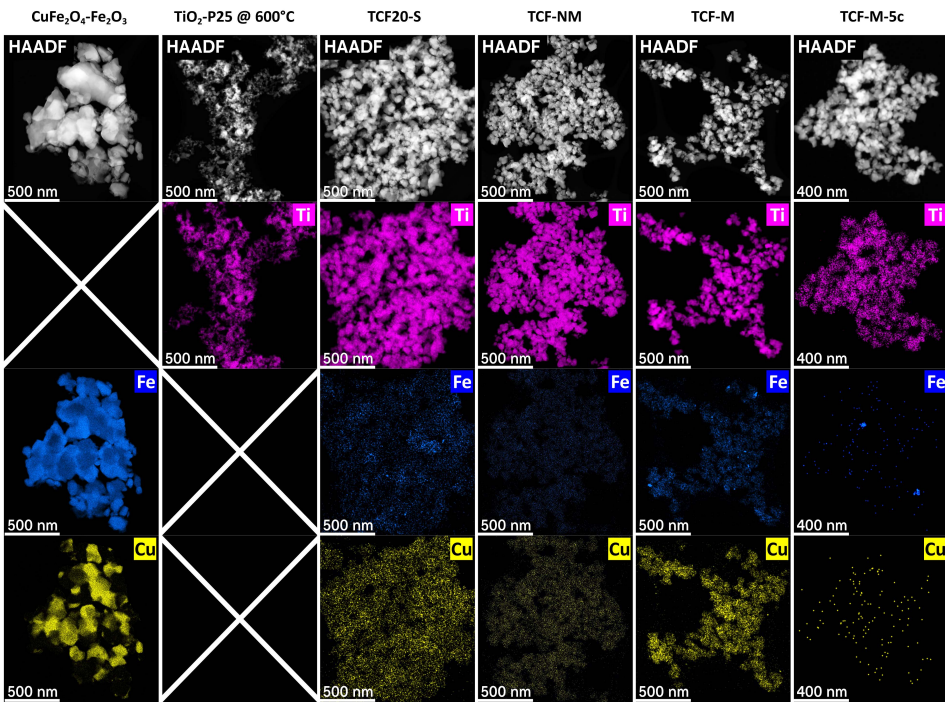


Figure 4. STEM-HAADF micrographs along with corresponding elemental maps of $\text{CuFe}_2\text{O}_4\text{-Fe}_2\text{O}_3$, $\text{TiO}_2\text{-P25 @ 600}^\circ\text{C}$, TCF20-S, TCF-NM, TCF-M, and TCF-M-5c. Figure reprinted by CC BY-NC 3.0 Deed licence from **Paper I**.

The crystal phase of the materials was characterized using XRD. According to XRD, annealing the TiO₂-P25 at 600 °C resulted in partial TiO₂ crystal phase transformation from anatase to rutile. The anatase to rutile ratio in the annealed material was close to 1. Indeed, anatase to rutile phase transformation temperature is known to be in the temperature range from 600 to 900 °C [25].

The XRD pattern of CuFe₂O₄-Fe₂O₃ show the presence of three major phases, hematite (α -Fe₂O₃), CuFe₂O₄ spinel and maghemite (γ -Fe₂O₃), along with minor phase such as α -SiO₂. The source of α -SiO₂ could be impurities in precursor materials (Table 3). The predominant phase in TCF20-S (Fig. 5) was rutile. The other phases in this material were anatase, hematite, CuFe₂O₄ spinel, and maghemite.

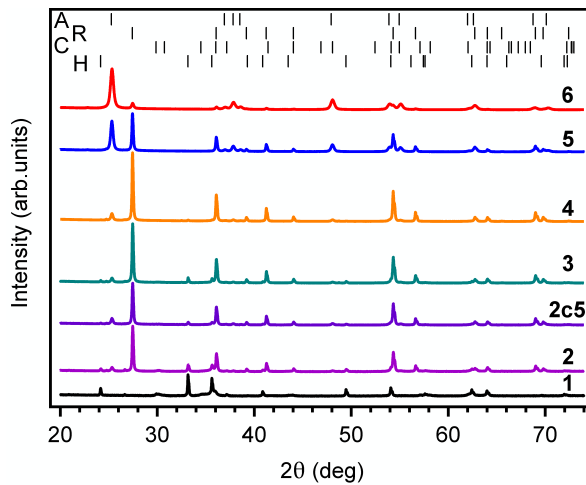


Figure 5. XRD patterns of **1** – CuFe₂O₄-Fe₂O₃, **2** – TCF-M, **2c5** – TCF-M-5c, **3** – TCF20-S and **4** – TCF-NM, **5** – TiO₂-P25 @ 600 °C, **6** – TiO₂-P25. The positions of reflection of anatase (**A**), rutile (**R**), CuFe₂O₄ spinel (**C**) and hematite (**H**) are shown as vertical bars at the upper part of the figure. Figure reprinted by CC BY-NC 3.0 Deed licence from **Paper I**.

Magnetic extraction did not change the phase composition but only distribution. The TCF-M contained more hematite, but especially CuFe₂O₄ spinel and maghemite phases. Thus, TCF-M contained magnetic phases in higher concentration compared to TCF20-S. The residual TCF-NM composed mainly of rutile and anatase fractions, along with traces of hematite, CuFe₂O₄ spinel and maghemite (see Table 3). Those results strongly suggest that the process of magnetic extraction was efficient in a selection of the desired TCF-M materials.

XRD results of recycled TCF-M-5c revealed consistent phase composition with TCF-M, but with slightly higher rutile and CuFe₂O₄, suggesting stability and minimal changes in phase composition after five recycling cycles.

Table 3. Phase distribution and composition of pure TiO₂-P25, TiO₂-P25 @ 600°, CuFe₂O₄-Fe₂O₃, TCF20-S, TCF-NM, TCF-M and TCF-M-5c deduced from XRD data. R'_{wp} is the background excluded weighted residual error (R-factor) from Rietveld analysis [104]. The phases marked with “-” have shown concentrations with a low or under detection limit value (< 0.2 wt%). Table reprinted by CC BY-NC 3.0 Deed licence from **Paper I**.

Material	Crystal phase, wt%						R' _{wp} , %
	Anatase	Rutile	α -Fe ₂ O ₃	CuFe ₂ O ₄	α -SiO ₂	γ -Fe ₂ O ₃	
CuFe ₂ O ₄ -Fe ₂ O ₃	–	–	53.5	33.9	1	11.6	13.7
TiO ₂ -P25	88.9	11.1	–	–	–	–	10.3
TiO ₂ -P25 @ 600 °C	51	49	–	–	–	–	7.7
TCF20-S	6.3	84.5	5.7	2.6	0.3	0.6	6.3
TCF-NM	10.8	87.2	0.9	0.5	0.2	0.4	6.1
TCF-M	6.7	69.6	12.4	8.8	1	1.5	7.2
TCF-M-5c	6.3	88.4	5.7	3.2	0.4	–	6.4

To obtain information on elemental oxidation states of the very top layer of the materials' surface, XPS measurements were conducted. According to XPS results all materials contained Ti in Ti⁴⁺ (Fig. 6 a) oxidation state [105, 106] and Fe in Fe³⁺ (Fig. 6 b) oxidation state [107, 108] expected. No Ti³⁺ or Fe²⁺ impurity contribution was found in any material.

Cu 2p photoelectron spectra are displayed in Fig. 6 c. The spectrum of CuFe₂O₄-Fe₂O₃ demonstrated a strong satellite line, characteristic of Cu²⁺ [109–111] – as expected for CuFe₂O₄. In the case of TCF20-S, TCF-NM, TCF-M and TCF-M-5c, the spectra contained one photoelectron line per spin-orbit component with a weak shoulder at the higher binding energy side, and the (Cu²⁺) satellite barely observable. Interestingly, the XPS spectrum of TCF-M-5c illustrated a further diminished presence of the Cu²⁺ satellite features, suggesting a reduced intensity of Cu 2p compared to the material before its photocatalytic degradation cycles. This finding suggested the formation of Cu¹⁺ at the surface of the material [110, 112]. However, this finding is contradictory to what XRD results demonstrated (see Table 3), as these did not indicate any phases related to Cu¹⁺. We, therefore, consider it plausible that the high Cu¹⁺/Cu²⁺ ratio we observe in XPS spectra is an effect of beam damage (reduction of Cu under irradiation of the XPS excitation source). Such a ‘beam damage’ effect in Cu²⁺ compounds has been previously reported by others under varied excitation sources [113]. We find such a scenario more plausible because we observed a slow degradation of the Cu²⁺ satellite intensity (relative to the main line) even when measuring the Cu 2p XPS of the TCF-M material.

Furthermore, the Cu L_{2,3} edge NEXAFS (see **Paper I**) of related materials (vide infra) all showed either pure or strongly dominant Cu²⁺ charge state.

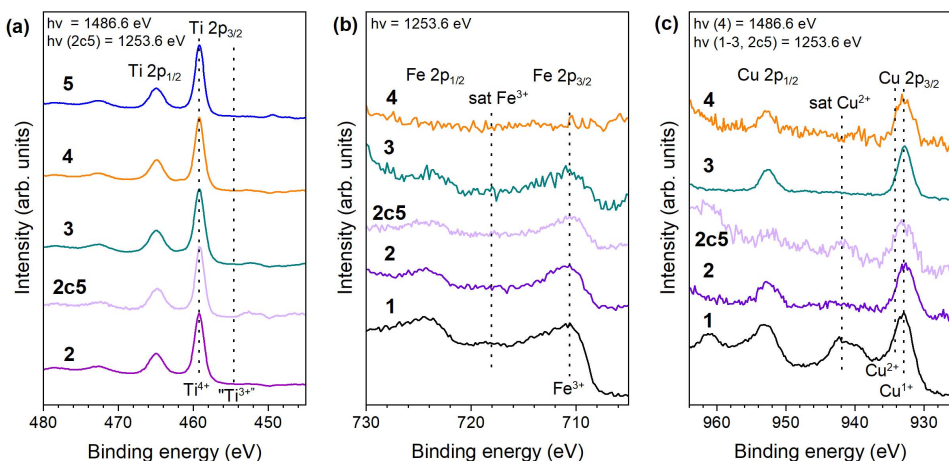


Figure 6. XPS spectra of the Ti 2p region (a), Cu 2p region (b) and the Fe 2p region (c) of **1** – $\text{CuFe}_2\text{O}_4\text{-Fe}_2\text{O}_3$, **2** – TCF-M, **2c5** – TCF-M-5c, **3** – TCF20-S, **4** – TCF-NM, **5** – $\text{TiO}_2\text{-P25 @ 600 }^\circ\text{C}$. Figure reprinted by CC BY-NC 3.0 Deed licence from **Paper I**.

The optical absorption spectra calculated from diffused reflectance spectra of all investigated materials are demonstrated in Fig.7. The absorption of $\text{TiO}_2\text{-P25}$ starts roughly at 400 nm, which aligns well with previous studies [114]. Absorption edges of TCF20-S, TCF-NM, TCF-M and TCF-M-5c are shifted towards longer wavelengths compared with $\text{TiO}_2\text{-P25}$ (see Fig. 7 a). The weak absorption at 560 nm is close to the band gap edge in hematite, maghemite and CuFe_2O_4 [106].

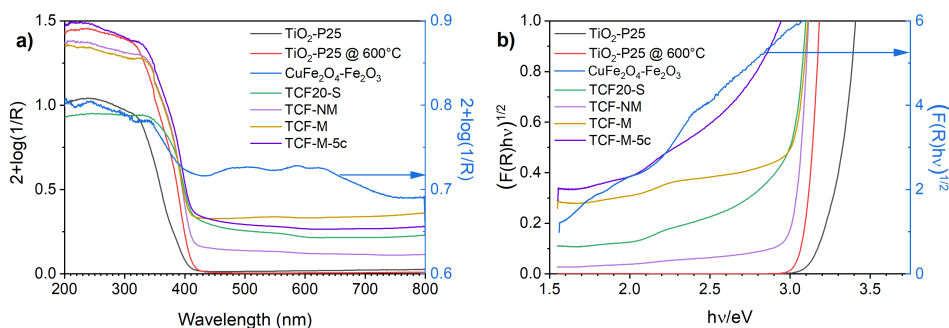


Figure 7. The UV-vis absorption spectra of $\text{TiO}_2\text{-P25}$, $\text{CuFe}_2\text{O}_4\text{-Fe}_2\text{O}_3$, TCF20-S, TCF5-NM, TCF-M and TCF-M-5c materials. (a) Full spectra and (b) spectra plotted as $(F(R)/h\nu)^{1/2}$ versus photon energy graphs. Spectra for $\text{CuFe}_2\text{O}_4\text{-Fe}_2\text{O}_3$ (blue lines) are zoomed, and respective y-axes on the right side are plotted in blue. Figure reprinted by CC BY-NC 3.0 Deed licence from **Paper I**.

Bandgaps were estimated from the diffuse reflectance data, the materials were analysed by using the Kubelka-Munk (K-M) theory. $\text{TiO}_2\text{-P25 @ 600 }^\circ\text{C}$ material has an absorption threshold of 3.12 eV, which aligns well with previous studies [114]. The $\text{CuFe}_2\text{O}_4\text{-Fe}_2\text{O}_3$ had several absorption thresholds since it was com-

posed of α - Fe_2O_3 , γ - Fe_2O_3 and CuFe_2O_4 spinel (Fig 7 b, blue line). The bandgap of hematite was 2.1 eV, which qualitatively agrees with an earlier theoretical estimate [115, 116]. TCF20-S had an absorption threshold of 2.97 eV, TCF-NM of 3.03 eV and TCF-M of 3.0 eV. The TCF20-S, TCF-M and TCF-M-5c had an additional absorption threshold at 2.1 eV, which was related to α - Fe_2O_3 . This result provides proof that materials absorb more visible light compared to pure TiO_2 -P25.

Photocatalytic activity

Photocatalytic activity of pure TiO_2 -P25, TiO_2 -P25 @ 600 °C, CuFe_2O_4 - Fe_2O_3 , TCF20-S, TCF-NM and TCF-M measured as degradation of model herbicide pollutant 2,4-D is demonstrated in Figure 8. The performance of pure 2,4-D provided a baseline for comparison, indicating the potential decay of this mode pollutant under UVA light. According to our results, 2,4-D was stable under UVA, and only slight (10%) degradation was observed after prolonged (18 h) irradiation. It is important to note that in our experimental set-up photocatalytic activity was measured without any stirring and with the studied materials placed on the surface of the 2,4-D solution. Such a set-up may result in lower photocatalytic activity than one would achieve with stirring. However, degradation of 2,4-D was well detectable with all the tested materials (see **Paper IV**).

The photodegradation process of 2,4-D is relatively well described and involves a transformation of 2,4-D into chlorinated intermediates and then into compounds like 1,2,4-benzenetriol and chlorohydroquinone, which undergo ring-opening and hydrolysis reactions catalysed by the TiO_2 surface, leading to complete mineralisation into carbon dioxide, water, and gaseous products [65, 117, 118].

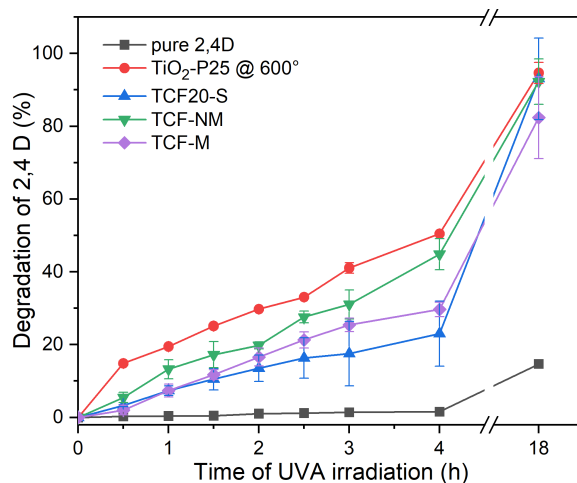


Figure 8. Photocatalytic degradation of 2,4-D in aqueous solution over time under UVA irradiation by various photocatalytic materials: TCF20-S, TCF-M, TCF-NM and TiO_2 600 °C. In addition, the degradation of a pure 2,4-D aqueous solution is shown. Figure reprinted by CC BY-NC 3.0 Deed licence from **Paper I**.

Photodegradation of 2,4-D by pure TiO₂-P25 was not assessed due to opacity of the respective suspension but TiO₂-P25 @ 600 °C demonstrated the highest degradation rate across all materials, achieving 20% loss of 2,4-D within 1 h, 50% loss of 2,4-D within 4 h and nearly complete degradation of 2,4-D (around 94.6%) after 18 h (Fig. 8). Within the first 1.5 h of UVA irradiation, both TCF20-S and TCF-M materials exhibited comparable degradation rates. After this time frame, magnetically extracted TCF-M material showed a higher rate of degradation, achieving 29.6% of 2,4-D degradation by 4 h, whereas the TCF20-S reached a slightly lower level of degradation by the same time. TCF-NM material demonstrated relatively good results, degrading 16% of 2,4-D within 1 h and 45% of 2,4-D degradation within 4 h and nearly complete degradation of 2,4-D (around 93%) after 18 h.

The superior photocatalytic activity of pure TiO₂-P25 @ 600 °C when compared with TCF20-S, TCF-M, and TCF-NM materials can be attributed to its relatively high anatase content while in the case of the latter TiO₂ has mostly rutile crystal structure (see Table 3). Therefore, from photocatalytic activity results, the photocatalytic component in the synthesized materials is TiO₂, and CuFe₂O₄-Fe₂O₃ works as a magnetic addition. TCF-M exhibits lower photocatalytic activity as it contains 20% less photocatalytic material than pure TiO₂-P25 @ 600 °C.

In Fig.9. the photocatalytic activity of TCF-M after five cycles (use and magnetic extraction) is demonstrated. Only a slight decrease in the photocatalytic degradation rate through subsequent cycles was observed, while the photocatalytic efficiency of this material remains commendably high. This stability of photocatalytic and 2,4-D degrading activity of TCF-M material after repeated use and collection from water strongly recommends the potential of this material as a reliable and practical choice for water purification applications, including recyclability.

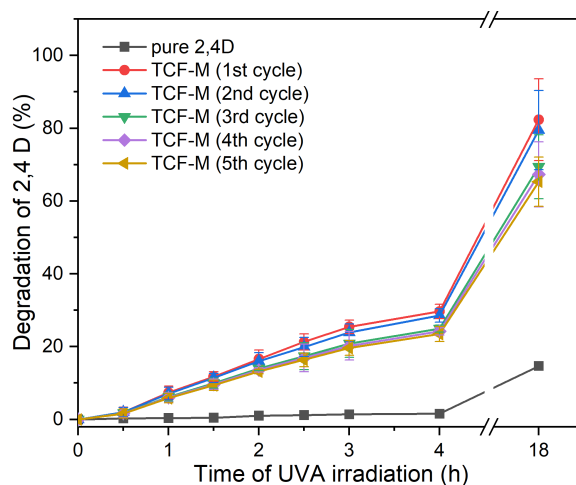


Figure 9. Time-dependent photocatalytic degradation of 2,4-D in aqueous solution using TCF-M, under UVA irradiation, after five cycles of use. For comparison, the degradation trend of a pure 2,4-D aqueous solution is also depicted. Figure reprinted by CC BY-NC 3.0 Deed licence from **Paper I**.

In conclusion, magnetically extracted material (TCF-M) demonstrated photocatalytic activity toward to hardly degradable herbicide 2,4-D. It needed only 20% of magnetic material to make TiO₂-P25 collectable. The material preserved crystal structural integrity and photocatalytic activity after 5 cycles of reusing and washing. The results of this research (**Paper I**) demonstrated that magnetically collectable photocatalytic materials can be efficiently removed from cleaned water.

5.2 ZnO and ZnO/Ag based photocatalytic coatings

Surface is the outermost layer of the material, where all the interactions between material and environment take place [119]. This section is dedicated to research of coatings where ZnO and ZnO/Ag are embedded into commercial matrix to form photocatalytic coating on solid surfaces. Furthermore, the influence of wear and tear on photocatalytic efficacy of the developed surface coatings was evaluated.

5.2.1 Nano-ZnO and nano-ZnO/Ag based photocatalytic coatings (Paper II)

ZnO has received attention as an alternative photocatalyst to TiO₂ [13]. However, it has a wide bandgap, about 3.37 eV [33], which makes it efficient only under UVA irradiation. To enhance ZnO UVA photocatalytic activity further it has been combined with noble metals such as Ag [12]. The noble metals deposited on the surface of ZnO can form the Schottky barrier, which enhances the charge separation and thus electron and hole lifetimes [12].

Furthermore, ZnO with deposited Ag nanoparticles can have application as photocatalytic antimicrobial coating since it generates reactive oxygen species, which efficiently attack all kind of organic molecules (including dead/alive bacteria membrane). Nano-ZnO/Ag also releases Ag and Zn ions, which are toxic to microorganisms.

In this chapter we demonstrate morphology, photocatalytic activity and surface wettability of novel coating based on nano-ZnO and nano-ZnO/Ag in commercial acrylic matrix on plywood.

Characteristics of coatings

The SEM-HAADF was used to image the morphology and elemental composition of the nano-ZnO/Ag (Fig. 10). The even distribution of Zn and O across the rod-shaped nanoparticles confirms their ZnO composition. The localization of Ag nanoparticles indicates that the silver predominantly adheres to the surfaces of the larger ZnO nanoparticles, aligning with expectations.

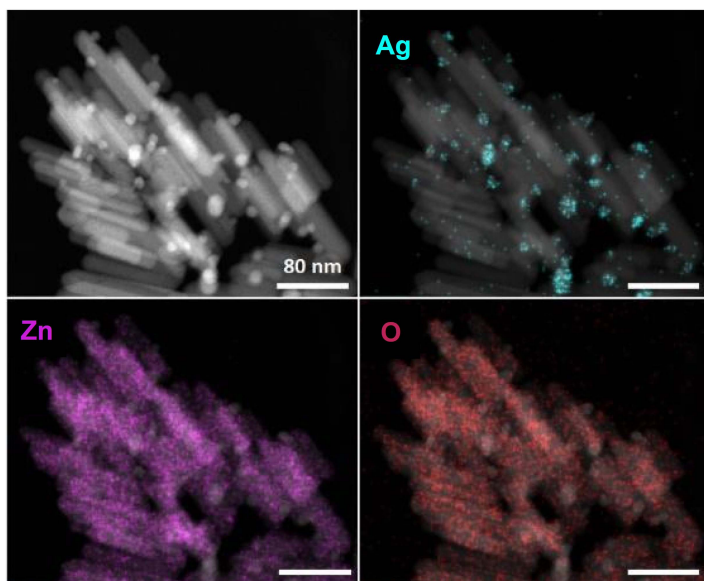


Figure 10. STEM-HAADF micrograph combined with corresponding elemental map of ZnO/Ag. Figure reprinted by CC BY-NC 3.0 Deed licence from **Paper II**.

The photographic top views of coated plywood samples display a more pronounced yellow colour in nano-ZnO/Ag-based coatings compared to those with nano-ZnO-only and pure matrix material. (Fig. 11 a)

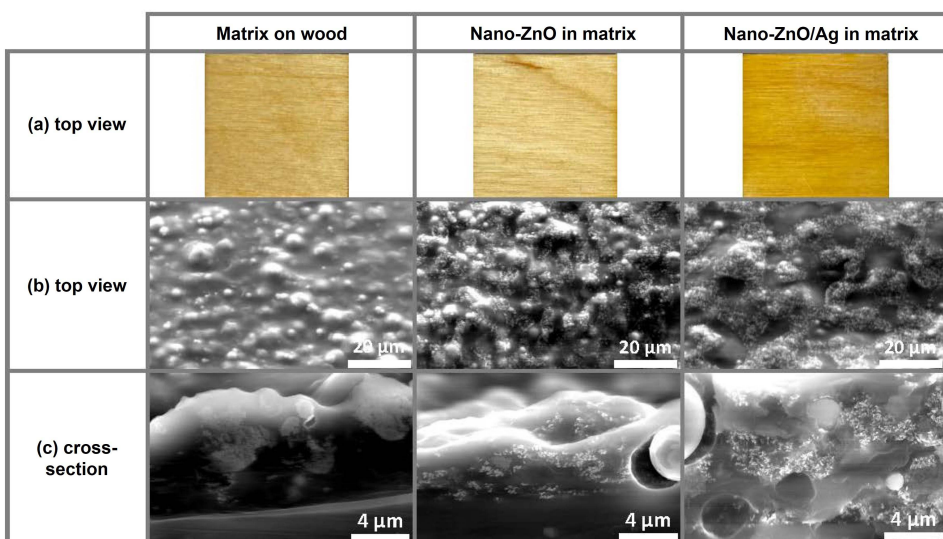


Figure 11. (a) Photographic top views of 25×25 mm samples on plywood. (b) top view and (c) cross-sectional SEM images of both nano-ZnO and nano-ZnO/Ag. Figure reprinted by CC BY-NC 3.0 Deed licence from **Paper II**.

SEM was used to demonstrate morphology and cross-section of nano-ZnO and nano-ZnO/Ag containing coatings on plywood (Fig. 11 b, c). Nano-ZnO and nano-ZnO/Ag-embedded nanoparticles have a comparable distribution on surface. Cross-sectional SEM images demonstrate that the nano-ZnO and nano-ZnO/Ag nanoparticle dispersion within the nanoscale is not entirely uniform. Due to the relatively high viscosity of the acrylic matrix material precursor even before drying, a completely uniform nanoparticle distribution is not expected.

XPS was used to characterize the surface composition and valence states of elements in surface coating (measurement depth 2–4 nm). The composition was evaluated from the overview spectra of nano-ZnO- and nano-ZnO/Ag-containing surface coatings on plywood (Fig 12 a). The overview spectrum of nano-ZnO/Ag-containing coatings demonstrated the presence of Zn, O, N, Cl, C and Si, as expected. However, Ag 3d photoelectron lines were not observed. This is due to the very small amount of silver, which is below XPS detection level (roughly 0.1 atomic percent).

In Table 4 the atomic concentrations of elements in nano-ZnO- and nano-ZnO/Ag-containing coatings on wood substrates according to XPS analysis. For comparison, similar data for pure matrix material on wood substrate are given. XPS of nano-ZnO/Ag does not show Ag photolines, due to the insufficient sensitivity of the XPS, as discussed above. Both samples had similar surface composition.

High-resolution Zn 2p XPS spectra of nano-ZnO and nano-ZnO/Ag coatings are shown in Fig. 12 b. According to the Zn 2p line positions and shape, it can be concluded that Zn is in the Zn²⁺ oxidation state, as expected in the case of ZnO.

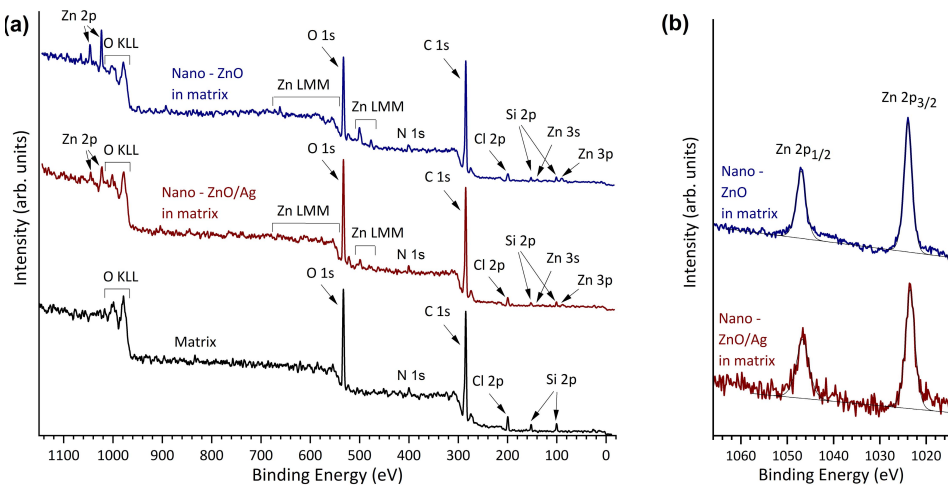


Figure 12. (a) XPS overview spectra and (b) Zn 2p XPS spectra of nano-ZnO- and nano-ZnO/Ag-containing coatings and pure matrix material on plywood substrates. According to the Zn 2p photoline positions and shape, Zn is in 2⁺-oxidation state. Figure reprinted following CC BY 4.0 Deed licence, from **Paper II**.

Ar⁺ sputtering was used to remove surface layers of the acrylic matrix to investigate possible buried Ag nanoparticles on ZnO (Fig. 13). No Ag signal was detected before and after Ar⁺ sputtering, i.e., “as prepared” and after the removal of the topmost layer of material with Ar⁺ ion bombardment. This is likely due to the insufficient sensitivity of XPS to the low levels of Ag present in the nano-ZnO/Ag.

Table 4 demonstrates the atomic concentrations of elements in nano-ZnO- and nano-ZnO/Ag-containing coatings on wood substrates according to XPS analysis. For comparison, similar data for pure matrix material on wood substrate are given.

Table 4. Atomic concentration of elements in nano-ZnO- and nano-ZnO/Ag-containing coatings and in pure acrylic matrix material on plywood substrates according to XPS analysis.

Element	C	O	Zn	Cl	Si	Ag	N
Nano-ZnO/Ag in matrix	70.6	21.3	0.5	1.6	3.5	not detected	2.5
Nano-ZnO in matrix	74.6	18.3	0.7	1.9	2.7	not measured	1.8
Matrix	69.6	23.4	not measured	2.4	3.5	not measured	1.1

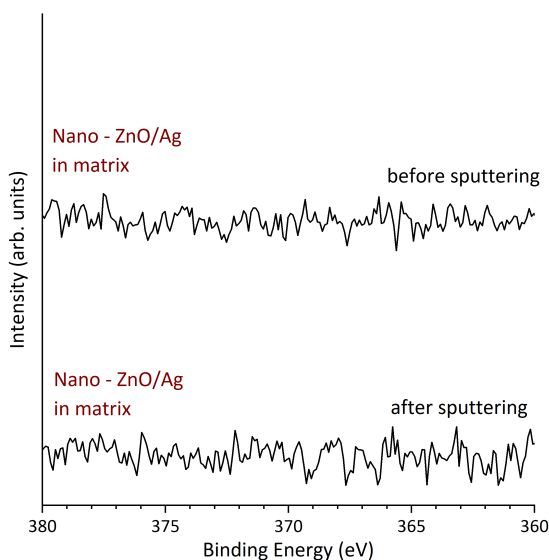


Figure 13. XPS spectra of nano-ZnO and nano-ZnO/Ag-containing coating and pure matrix material on wood substrate. Spectral region respective to Ag 3d photoline of nano-ZnO/Ag-containing coating on wood substrate before and after Ar⁺ sputtering. No Ag signal was detected since the amount of silver was below the detection limit of XPS. Figure reprinted following CC BY 4.0 Deed licence, from **Paper II**.

The water contact angle measurements provided insights into the hydrophobicity of ZnO and ZnO/Ag containing surfaces in as prepared form and after up to ten reuse cycles (Fig. 14). Initially, all surfaces exhibited high contact angles, indicative of substantial hydrophobicity. However, a notable decrease in hydrophobicity was observed after undergoing 5 cycles of reuse, which included organic soiling and wiping. After 10 reuse cycles, the contact angles decreased by approximately 10° to 13° across all surfaces, including the controls. This reduction suggests an increase in surface hydrophilicity, attributed primarily to changes in the matrix material rather than the incorporated nanoparticles. This shift towards greater hydrophilicity with repeated use reflects the impact of the wear regimen on the surface characteristics, emphasizing the durability and adaptability of the surface coatings under practical conditions. The observed change was low thus suggesting good durability of the coating.

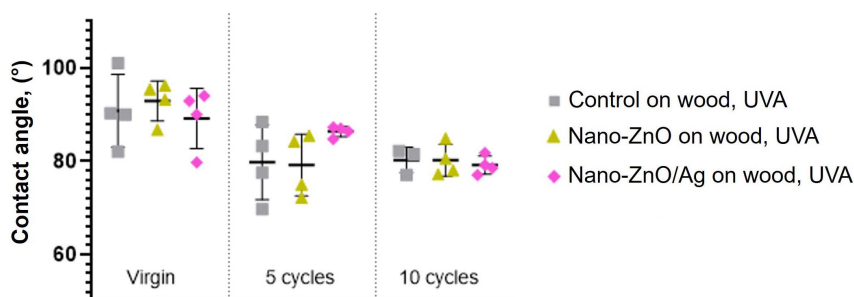


Figure 14. Contact angle measurements of surfaces in as prepared form (virgin surfaces) and after reuse cycles. Mean value of 3 experiments \pm SD is presented. Figure reprinted following CC BY 4.0 Deed licence, from **Paper II**.

Photocatalytic activity

Prior to testing of antimicrobial effect, photocatalytic activity of ZnO and ZnO/Ag covered surfaces was evaluated using organic dye MB. Photocatalytic efficacy was considered also as a proxy for antimicrobial efficacy of the surfaces.

For the photocatalytic experiments (Fig. 15), glass surfaces coated with film of nano-ZnO and nano-ZnO/Ag particles served as nanomaterial controls. This setup was used to assess the essential photocatalytic efficiency of the nanoparticles without any matrix interference. Both nano-ZnO and nano-ZnO/Ag on glass demonstrated similar high activity, achieving higher than 90% degradation of MB dye after 240 min under UVA irradiation. In the case of nano-ZnO and nano-ZnO/Ag photocatalytic coating with acrylic matrix degradation efficiency after 240 min dropped to 43% and 45% respectively. It was only after 720 min degradation rate of dye by nano-ZnO/Ag on wood surface matched that of the nano-ZnO/Ag without the matrix (on glass). Interestingly, surfaces with acrylic matrix embedded nano-ZnO/Ag appeared to enhance the photocatalytic performance compared to surfaces with nano-ZnO alone.

The photocatalytic test provided a crucial understanding of photocatalytic nano-ZnO and nano-ZnO/Ag, both with acrylic matrix and without (on glass). These assays set the foundation for subsequent antimicrobial evaluations, as shown in more detailed **Paper II**. The surfaces based on matrix-embedded nano-ZnO and nano-ZnO/Ag demonstrated substantial antibacterial activity under UVA illumination in standard wet conditions (see **Paper II**).

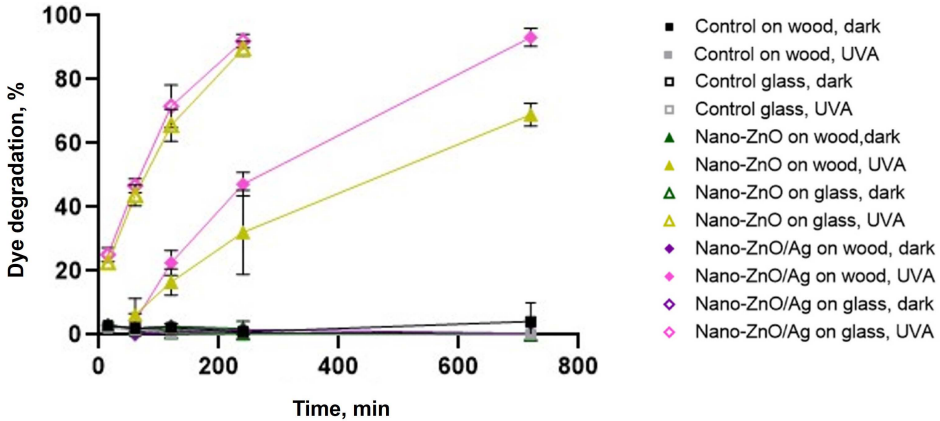


Figure 15. Photocatalytic dye degradation is shown to demonstrate differences in photocatalytic efficiency of the studied surfaces. Mean value from 3 experiments \pm SD is presented. Figure reprinted following CC BY 4.0 Deed, from **Paper II**.

5.2.2 Impact of wear and tear on photocatalytic ZnO surface coatings (Paper III)

In the previous chapter photocatalytic efficiency of coating based on nano-ZnO in commercial acrylic matrix were demonstrated. However, in order to apply these surfaces in real life conditions not only its efficiency but stability and durability are important.

Many research groups are focusing on mechanical durability of surfaces/coatings, but not onto preservation of its photocatalytic or antimicrobial property [120, 121]. There are a variety of methods to test the surface coatings and simulate wear. These include cross-cut method, pencil hardness test, rotary platform test, and impact tests [122–124]. The simplest and most widely used tribology test is sandpaper abrasion with specified weight, fixed speed, and distance [91]. However, there is lack of clear performance criteria and appropriate standard testing methods for photocatalytic and antimicrobial surfaces.

In this chapter three different treatments were performed to evaluate the durability of micro- ZnO micro- and nanostructures-based surface coatings after simulated wear. To investigate the changes in photocatalytic activity of ZnO in commercial acrylic matrix we prepared surfaces on stainless steel. Stainless steel is a common material used outdoors. In this chapter we demonstrate the relationship of durability and photocatalytic activity together with surface wettability on coatings based on ZnO in commercial acrylic matrix.

Characteristics of surfaces

To assess the physical changes in surface coatings during simulated wear, SEM was employed. The initial observation showed that the acrylic matrix or ZnO-infused acrylic matrix coatings on SS had small surface roughness but slightly uneven, as expected for a matte surface topcoat. No visible ZnO particles indicated from the topmost layer of ZnO-containing coatings, suggesting that the outermost layer was composed of the matrix polymer. This aligns with the understanding that the smoothness of polymer surfaces is heavily influenced by the ratio of pigment to polymer; lower ratios typically result in smoother surfaces.

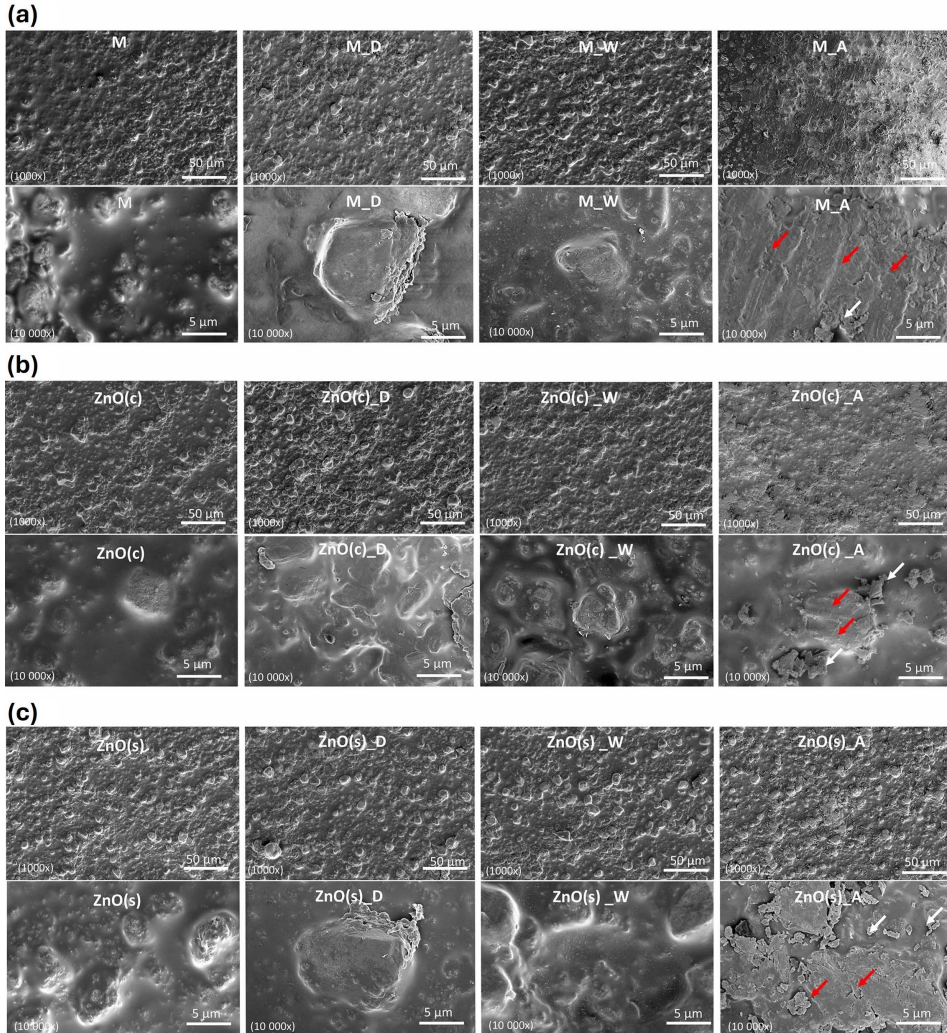


Figure 16. SEM images of surface coatings. (a) Acrylic topcoat matrix covered surfaces, (b) ZnO(c) in acrylic topcoat matrix surfaces, (c) ZnO(s) in acrylic topcoat matrix surfaces. Untreated surfaces (left column) and surfaces treated with dry (D) or wet (W) rubbing and abrasive treatment (A) procedures were viewed using 1000× [upper rows of (a)–(c)] and 10,000× [lower rows of (a)–(c)] magnification. Red arrows indicate visible scratches and white arrows indicate released surface coating material. Figure reprinted following CC BY 4.0 Deed, from **Paper III**.

The wear simulation treatments led to noticeable alterations in all surface coatings. At 1000× magnification, SEM revealed distinct changes for samples subjected to abrasive treatments (Fig. 16 a–c, upper rows). Visible scratch marks were seen, and parts of the uppermost matrix polymer were stripped away, flattening the original surface texture. These scratch marks (indicated by red arrows in Fig. 16) correspond to imprints from the abrasive pad used. Further examination at 10,000 × magnification showed that every type of treatment caused changes to the surface coatings. Materials from the coatings, whether acrylic matrix polymer or embedded ZnO micro- and nanostructures, were displaced and accumulated around the edges or spread across the surface, depending on whether the treatment was dry or wet rubbing.

Interestingly, nevertheless, contact angle measurements showed that surface hydrophobicity was unaffected by the formation of scratch marks and the release of surface material (Fig. 17).

The contact angles for all types of surface treatments consistently exceeded 90°, categorizing them as hydrophobic. The hydrophobic or hydrophilic nature of surfaces is typically influenced by their topographical structure and chemical composition. Given that our experimental conditions, including abrasion, did not alter the contact angles, we can conclude that the hydrophobic or hydrophilic characteristics of these surfaces are primarily determined by their chemical composition.

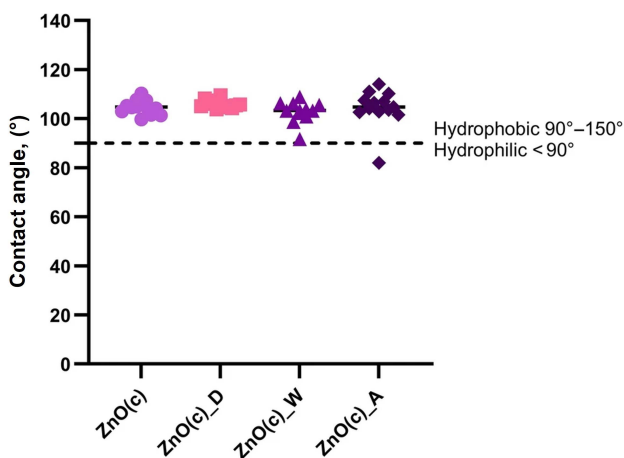


Figure 17. Contact angles of surface coatings before and after treatment. ZnO(c) in acrylic matrix surfaces were used as a model surface in untreated form or after dry (D) or wet (W) rubbing or abrasive treatment (A). Single measurement values and averages are shown. The dashed line represents 90° contact angle above which surfaces were considered hydrophobic. Figure reprinted following CC BY 4.0 Deed, from **Paper III**.

Photocatalytic activity

Under UVA illumination, ZnO-based surface coatings demonstrated a significant photocatalytic effect after 4 h of UVA irradiation, as depicted in Fig. 18 a. The results, further detailed in Fig. 18 b, show no discernible differences in the photo-

catalytic activity between surfaces containing ZnO(c) microparticles and ZnO(s) nanoparticles. The matrix alone also exhibited some photocatalytic activity, likely due to the light-induced degradation of MB dye, though this effect was substantially weaker compared to the ZnO-based coatings.

Previous studies, including those where ZnO powder was immobilized in acrylic paint for indoor decorative applications, corroborate the robust photocatalytic effects observed in our ZnO-based coatings [125, 126]. Similarly, Vu et al. reported that both nanoparticle- and microparticle-based ZnO coatings exhibit photocatalytic activity, with a reduced effect noted in neat coatings [126], as illustrated in Fig. 18 a b.

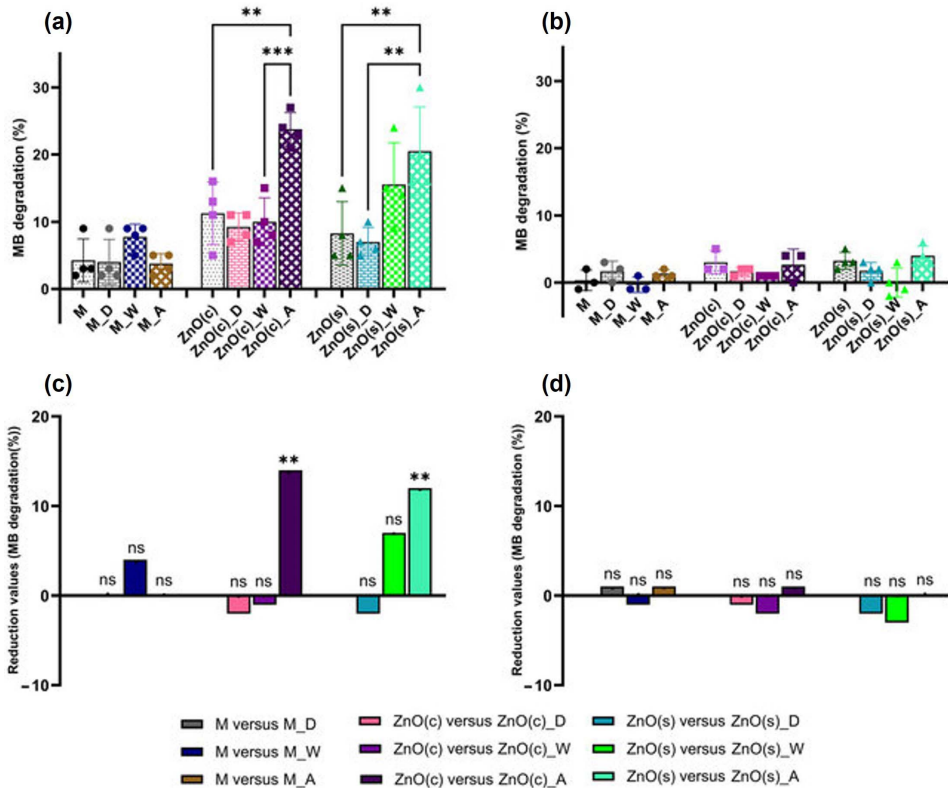


Figure 18. Photocatalytic activity of surface coatings before and after treatments. Photocatalytic activity was assessed through the degradation of MB dye across different coatings: matrix alone (M), ZnO(c) or ZnO(s) surface coatings after dry (D) or wet (W) rubbing or abrasive treatment (A). (a) Photocatalytic activity under UVA and (b) photocatalytic activity in dark conditions. Lower graphs represent the differences in MB degradation between surfaces treated by D, W, or A and the untreated surface under UVA (c) or in the dark (d). Color codes used on (c) and (d) are shown. Datapoints and the average of four parallels with standard deviation are shown. Statistically significant differences ($p < 0.05$) are shown as: ns—nonsignificant, ** ($p < 0.01$), *** ($p < 0.001$). Figure reprinted following CC BY 4.0 Deed, from Paper III.

In evaluating the impact of different surface treatment methods, our findings reveal that only abrasive treatment significantly enhanced the photocatalytic activity of ZnO-based coatings, as illustrated (Fig. 18 a c). Conversely, dry and wet rubbing treatments did not affect the MB degradation profile of any coatings, aligning with previous observations that these methods do not facilitate the release of Zn ions or ZnO particulates, unlike abrasive treatment (see **Paper III**).

The improved photocatalytic performance following abrasive treatment suggests that the material released from the coatings – predominantly photocatalytically active ZnO particulates, visible in SEM images (Fig. 16) – plays a crucial role. Further investigation into abrasively treated surfaces identified protruding ZnO particulates, which likely contributed to the observed increase in photocatalytic activity, as depicted (Fig. 18 b). These findings underscore that while abrasive treatment can significantly boost the photocatalytic and self-cleaning capabilities of ZnO-based acrylic matrix coatings, it may also reduce the coatings' durability.

In conclusion, this comprehensive analysis suggests that while certain treatments can enhance functional properties like photocatalysis, they may also pose challenges to the structural integrity and longevity of the coatings, underscoring the need for a balanced approach in the practical application of these materials.

5.3 Photo-induced effects of commercial photocatalytic SaniTise™ and BIOCLEAR®-window glasses (Paper IV)

Since the discovery of TiO₂ photocatalytic property, extensive work has been carried out by academia and industry to apply those materials in real life conditions [127]. It was the discovery of light induced hydrophilicity of TiO₂ surfaces which made it possible to manufacture self-cleaning and now antimicrobial coating for glass.

Antimicrobial glass has photocatalytic and light-induced hydrophilic coating that provides antimicrobial properties. One of the first antimicrobial glass was developed by Pilkington and their product is called as SaniTise™ [128]. Soon after the other companies followed with their own products such as Saint-Gobain with its BIOCLEAR®.

In this chapter photocatalytic property of commercially produces surfaces SaniTise™, BIOCLEAR® and as a control PLANICLEAR® (original glass, without TiO₂ on its surface) were investigated. In the focus of the thesis was relationship between photocatalytic activity and wettability of SaniTise™ and BIOCLEAR® with and without UVA pre-activation.

Characteristics of surfaces

Commercial producers of SaniTise™ and BIOCLEAR® glass surfaces claim that their products feature a TiO₂ coating. XPS for analysing the elemental composition and chemical state of these TiO₂-coated glass surfaces.

Surface composition analysis of the uppermost region (6 ± 2 nm) of glasses with XPS revealed distinct spectra with O 1s and Ti 2p photoelectrons, confirming the presence of TiO_2 [112] on both SaniTise™ (Fig. 19 a, b) and BIOCLEAR® (Fig 19 c, d) glass coatings. No other Ti oxidation states or chemical species besides TiO_2 were detected in the high-resolution Ti 2p spectra (Fig. 19 b, d) [113].

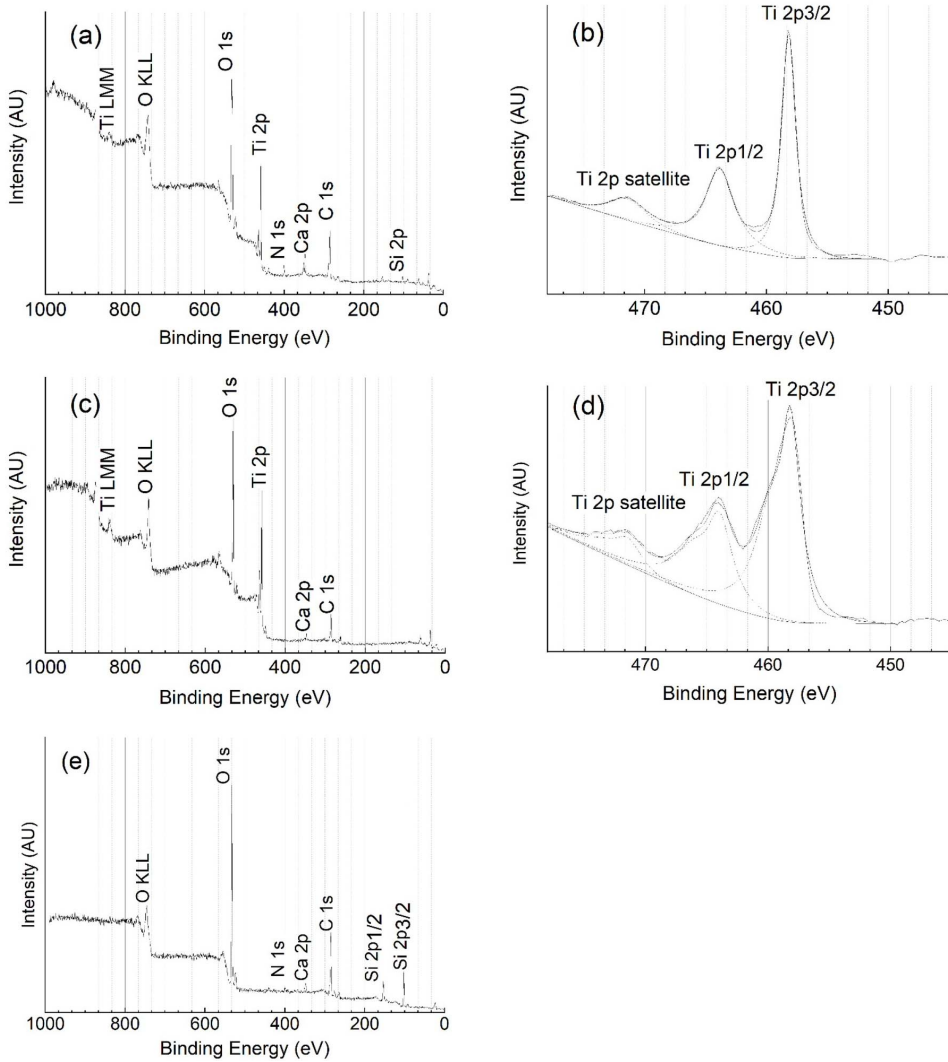


Figure 19. XPS survey spectra of (a) SaniTise™, (c) BIOCLEAR®, and (e) control (uncoated side of BIOCLEAR® glass). Ti 2p high-resolution spectra of (b) SaniTise™ and (d) BIOCLEAR®. Dotted lines represent the spectral components of experimental spectra obtained by fitting. XPS photoelectron lines are marked as element symbols and respective core levels. Auger peaks are marked as element symbols and Auger transition series. Spin orbitally split Ti 2p photoline sub-bands are marked as Ti 2p_{3/2} and 2p_{1/2}. The TiO_2 shake up satellite is marked as well. Modified figure following CC BY 4.0 Deed, from **Paper IV**.

Notable, the peak asymmetry in the Ti 2p spectrum of the BIOCLEAR[®] glass surface (Fig. 19 d) can be explained by charging effects. The survey spectra of SaniTise[™] and BIOCLEAR[®] glass surfaces indicated that both surfaces contain Ti, O, C, and C (Fig 18 a). Additionally, SaniTise[™] survey spectrum also demonstrates Si. As expected, the reference spectrum for the uncoated side of the BIOCLEAR[®] glass displayed only the presence of O, C, Si, and Ca (Fig. 19 e). We suggest that Ca on the surface of BIOCLEAR[®] and SaniTise[™] glass originated from Ca ions diffused from the base glass substrate.

The presence of light-induced superhydrophilicity is an important feature for distinguishing ordinary glass from photocatalytically active glass, which can be used for antimicrobial applications on the internal surfaces of buildings. Measurement of light-induced hydrophilicity can explain photocatalytic properties of a surface. The hydrophilicity of original (called also “virgin”) glasses and all the three glasses was measured before (“virgin” surfaces) and after UVA pre-activation. The concept of UV pre-activation of photocatalytic surfaces prior to their use is also included in internationally standardized procedures, e.g., in ISO 10678 [129].

In this experiment also PLANICLEAR[®] glass, that material-wise is similar to BIOCLEAR[®] but lacks the photoactive surface layer, was introduced. UVA pre-activation of SaniTise[™] and BIOCLEAR[®] clearly increased their hydrophilic properties (Fig. 20) and decreased the initial water contact angle of 60° to 20–30° after 4 h and to ≤10°, i.e., to superhydrophilic, after 24 h (Fig. 20 a). This suggests that the realization of superhydrophilicity and possible self-cleaning effect of anatase-TiO₂-based glass surfaces indeed requires UVA pre-activation. Interestingly, when UVA irradiation of SaniTise[™] and BIOCLEAR[®] was finished (i.e., after 72 h), the hydrophilicity of the glass surfaces was gradually lost (Fig. 20 b), and it reverted to its initial level 48 h after the end of pre-activation. UVA irradiation of PLANICLEAR[®] control glass did not cause any change in water contact angle (Fig. 20 a b).

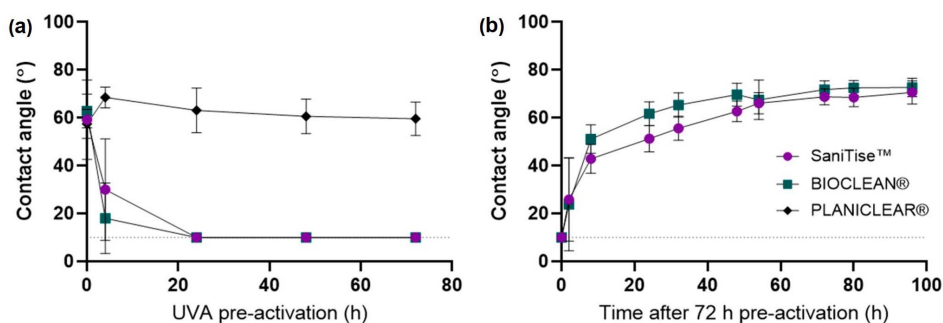


Figure 20. Time and treatment-dependent changes in hydrophilicity of the glass surfaces according to contact angle measurements: (a) contact angle variation after pre-activation with high-intensity (22–25 W/m²) UVA; (b) contact angle recovery in dark conditions (note that PLANICLEAR[®] control glass was not measured as there was no change in contact angle according to (a)). The dotted line represents an immeasurable contact angle value (10°), below which the surfaces were considered superhydrophilic. Figure reprinted following CC BY 4.0 Deed, from **Paper IV**.

Photocatalytic activity

In order to utilize the superhydrophilicity-related properties of SaniTise™ and BIOCLEAN® glasses, all the three glass types were tested for their photocatalytic activity and antibacterial effect in “virgin” form and also immediately after 72 h pre-activation.

Assuming that the antibacterial effect of SaniTise™ glass is directly related to its ability to produce reactive oxygen species due to UVA irradiation, we first determined the photocatalytic activity of all the glass surfaces in the dark and under UVA. Alternatively, BIOCLEAN® and SaniTise™ surfaces were also pre-activated under UVA as described above. Furthermore, to clarify the effect of UVA pre-activation on photocatalytic activity, the pre-activated surfaces were also recovered in the dark after pre-activation up to 72 both virgin and UVA pre-activated glasses were measured, and the latter were also evaluated for photocatalytic activity after their 2 h and 72 h recovery in the dark (Fig. 21). Surprisingly our results showed that, in general the studied glass surfaces had a very low photocatalytic effect in the experimental conditions used, except UVA pre-activated SaniTise™ glass (Fig. 21). Interestingly, this significant photocatalytic effect of SaniTise™ glass was retained after 2 h and 72 h dark recovery post pre-activation.

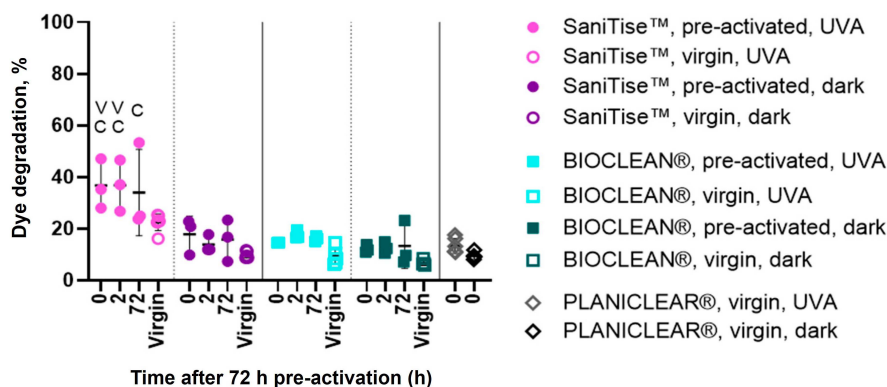


Figure 21. Photocatalytic effect of SaniTise™, BIOCLEAN®, and PLANICLEAR® (control) glasses according to 4 h methylene blue degradation assay. Virgin and UVA pre-activated glass surfaces (0 h: UVA pre-activated surface used immediately; “2”: 2 h recovery of the surface after pre-activation; “72”: 72 h recovery of the surface after pre-activation). The ‘V’ denotes a significant difference from the virgin surface of the same type in the same conditions ($p < 0.05$); ‘C’ denotes a significant difference from PLANICLEAR® control surfaces in the same conditions ($p < 0.05$). Figure reprinted following CC BY 4.0 Deed, from **Paper IV**.

Therefore, as expected, the photocatalytic effect of TiO₂-based surfaces and surface hydrophilicity determined by the contact angle method do not always coincide. The reason is that photocatalysis and hydrophilicity can take place simultaneously on the same surface, even though the mechanisms are completely different [130]. Photocatalysis involves the activation of the surface by light to initiate

chemical reactions that degrade contaminants, while hydrophilicity increases the surface's affinity for water, enhancing the cleaning process by spreading water more effectively over the surface. Intriguingly, BIOCLEAR[®] glasses that are advertised as photocatalytically active glasses did not cause any significant MB degradation in the experimental conditions. We suggest that one of the reasons behind such a difference is the thickness of TiO₂ layer on those different glasses, as shown by Raman analysis (see **Paper IV**). Expectedly, the PLANICLEAR[®] glass that served as a control also did not demonstrate any photocatalytic effect after UVA pre-activation and further UVA irradiation.

In conclusion, the contact angle measurement indicated increased surface hydrophilicity and reduced initial contact angle under UVA exposure for both SaniTise[™] and BIOCLEAR[®] glass, which are expected to exhibit high photocatalytic performance. However, the experiments showed that photocatalytic activity and surface hydrophilicity of SaniTise[™] and BIOCLEAR[®] (coatings based on TiO₂) do not always align. This is because photocatalysis and hydrophilicity can occur simultaneously on the same surface but are driven by different mechanisms. Additionally, SaniTise[™] demonstrated superior antibacterial activity (see **Paper IV**) compared to BIOCLEAR[®].

SUMMARY

This thesis is dedicated to the synthesis, development, characterization, photocatalytic efficiency and potential use of photocatalytic TiO₂- and ZnO-based materials for water treatment and antimicrobial applications.

In the focus of **Paper I** is magnetically collectable photocatalysts based on TiO₂-P25 for water treatment. A mixture of magnetic CuFe₂O₄-Fe₂O₃ and commercial TiO₂-P25 was annealed at 600 °C, to form a novel magnetically collectable photocatalyst (TCF-M). Magnetic material content in the mixture was 20%. For photocatalytic analysis, herbicide 2,4-D (dichlorophenoxyacetic acid) was chosen as a well-researched and stable pollutant, which is hardly degradable in water. Under UVA irradiation (2.5–3 W/m²), TCF-M reduced 30% of 2,4-D after 4 h and nearly 93% after 18 h. Annealed TiO₂-P25 degraded 2,4-D faster (50%) due to its higher anatase content (51%) compared to TCF-M (6.7%). Notably, 2,4-D did not degrade under UVA within 4 h without a photocatalyst. TCF-M preserved structural integrity, exhibited good reusability and collectability, losing only 20% efficiency after the initial two cycles of reuse, and maintained consistent degradation rate of 2,4-D up to five reuses. The results of this research demonstrated that magnetically collectable photocatalytic materials can be prepared and reused to remove organic contaminants from water.

Paper II was dedicated to research of ZnO and ZnO/Ag nanoparticle-based photocatalytic coatings for antimicrobial applications. First the photocatalytic activity of ZnO and ZnO/Ag nanoparticles powder (without matrix) on glass substrate was investigated and the MB degradation rate was found to be high, up to 90% within 4 h under UVA irradiation (2.5–3 W/m²). Then the nanoparticles were successfully incorporated into an acrylic matrix and the mixture was coated on plywood. The ZnO and ZnO/Ag nanoparticles were well-distributed in acrylic matrix and were present on the surface. The coatings exhibited 30% (ZnO) to 45% (ZnO/Ag) MB degradation under UVA in 4 h, showcasing their high photocatalytic activity. The study highlighted potential sustainable development of functional photocatalytic nanostructural coating materials.

In **Paper III** the impact of wear and tear on ZnO-based photocatalytic acrylic coatings on stainless steel was investigated. Three different surface treatments (wet, dry and abrasive) were performed to evaluate the durability of ZnO nanoparticle- and commercial ZnO microparticle-based acrylic coatings after simulated wear. SEM analyses confirmed smooth surface structure before treatment in case of both coatings and changes after abrasive treatment (marks, scratches). Prepared surfaces were hydrophobic and remained the same (contact angle > 90°) after simulated wear. However, photocatalytic activity of commercial and synthesized ZnO coatings, after wet and dry treatment showed approximately 10% MB degradation after 6 h of UVA irradiation (2.5–3 W/m²). Abrasive treatment improved degradation rate of MB to 25% under the same UVA exposure. Results demonstrated preserved photocatalytic activity (increased in case of abrasive treatment)

of ZnO nanoparticle- and commercial ZnO microparticle-based acrylic coatings under simulated wear and tear.

Paper IV of this thesis analyses commercially available TiO₂-based photocatalytic glasses, BIOCLEAN[®] and SaniTise[™], the latter also declared to have antimicrobial functionality. Glass surfaces exhibited moderate MB degradation of 20% and 40%, respectively, over 72 h under high-intensity UVA exposure (22–25 W/m²). Surface hydrophilicity increased with UVA pre-treatment, the initial water contact angle decreased from 60° to ≤10° after 24 h. However, the coatings lost hydrophilicity without continuous UVA irradiation. The results of this paper demonstrated that photocatalytic effect of TiO₂-based surfaces and surface hydrophilicity determined by the contact angle method did not coincide. The main reason is that photocatalysis involves the activation of the surface by light to initiate chemical reactions that degrade contaminants, while hydrophilicity increases the surface's affinity for water, enhancing the cleaning process by spreading water more effectively over the surface. SaniTise[™] demonstrated higher photocatalytic and antibacterial activity than BIOCLEAN[®], the latter being only marginally more active than control glass sample.

Overall, the approach used in this thesis was designed to encompass different aspects of the development and application of photocatalytic materials, enhancing the understanding of material composition and possible use. By developing innovative material compositions, such as the magnetically collectable CuFe₂O₄-Fe₂O₃ with TiO₂, the functionality and applicability of TiO₂ was advanced for water treatment. The photocatalytic activity of prepared nano-ZnO- and nano-ZnO/Ag-based acrylic coatings was evaluated to be similar to commercial TiO₂-based SaniTise[™] glass surface. Nano-ZnO-based acrylic coatings after simulated wear and tear preserved photocatalytic activity and thus are potentially applicable in real-life conditions.

Throughout this work, I have recognized the importance of the development of an effective photocatalyst and photocatalysis-based antimicrobial materials. Thereafter important are innovative material combinations, thorough material characterisation, optimization of material synthesis, efficacy of the materials as well as durability. Collectively, the materials developed within this PhD thesis show a significant potential as photocatalysts for water treatment and in photocatalytic antimicrobial coatings.

SUMMARY IN ESTONIAN

Fotokatalüütilised materjalid veepuhastuse ja antimikroobsete rakenduste jaoks

Käesolev doktoritöö on pühendatud TiO₂- ja ZnO-põhiste fotokatalüütiliste materjalide sünteesile, fotokatalüütilistele omadustele, karakteriseerimisele, arendamisele ja potentsiaalsele kasutamisele veepuhastuses ja antimikroobsetes rakendustes.

I artikli fookuses on TiO₂-P25 baasil valmistatud veepuhastuseks mõeldud magnetiliselt kokku kogutavad fotokatalüsaatorid. Seesuguste uudsete fotokatalüsaatorite (TCF-M) saamiseks sünteesiti magnetiline ühend CuFe₂O₄-Fe₂O₃, lisati seda kommertsiaalsele TiO₂-P25-le ning saadud segu lõõmutati 600 °C juures. Tuleb rõhutada, et magnetilise materjali sisaldus segus oli ainult 20% ning juba see tagas hea kokku kogutavuse. Fotokatalüütilise aktiivsuse analüüsiks valiti hästi uuritud ja stabiilne põllumajanduslik herbitsiid 2,4-D (diklorofenoksüädikhape), mis vees tavaoludes laguneb aeglaselt. UVA kiirgusega eksponeerimise korral (2.5–3 W/m²) vähenes 2,4-D kontsentratsioon TCF-M mõjul 4 h jooksul 30% ja 18 h jooksul ligi 93% võrra. Sellised tulemused olid pisut väiksemad kui võrdlusobjektiks olnud lõõmutatud TiO₂-P25 korral, mille puhul 4 h jooksul lagunes 50% 2,4-D-d. Lõõmutatud TiO₂-P25 lagundas 2,4-D kiiremini tänu selle suuremale anataasi sisaldusele (51%) võrreldes TCF-M-ga (6.7%). Oluline on lisada, et vesilahuses ei lagunenu 2,4-D UVA-ga eksponeerimisel 4 h jooksul ilma lisatud fotokatalüsaatorita. TCF-M säilitas kasutamisel ka struktuurse terviklikkuse ning demonstreeris head korduvkasutatavust ja magneti abil vedelikust kokku kogutavust. Seejuures vähenes TCF-M efektiivsus pärast esimest kahte korduskasutuse tsüklit vaid 20% ning saavutas 2,4-D vesilahuse puhul stabiilse lagundamiskiiruse viie tsükli jooksul.

Artikkel II oli pühendatud ZnO ja ZnO/Ag nanoosakestel põhinevate fotokatalüütiliste pinnakatete uuringutele antimikroobsete rakenduste jaoks. Esmalt uuriti ZnO ja ZnO/Ag nanoosakeste pulbri fotokatalüütilist aktiivsust (ilma maatriksita) klaassubstraadil ning leiti, et metüleensinise (MS) lagunemiskiirus on kõrge, kuni 90% 4 h jooksul UVA (2.5–3 W/m²) eksponeerimise korral. Seejärel segati nanoosakesed akrüülipõhisesse lakki ning segu kanti vineerile. ZnO ja ZnO/Ag nanoosakeste karakteriseerimine viidi läbi STEM-EDX-ga ning nende jaotust akrüülmaatriksis uuriti SEM ja XPS meetoditel. Akrüülipõhised nanoosakestega pinnakatted demonstreerisid UVA-ga eksponeerimise korral 30% (ZnO) kuni 45% (ZnO/Ag) MS fotokatalüütilist lagunemist 4 h jooksul. Antud uuring demonstreerib selgelt funktsionaalsete fotokatalüütiliste nanostruktuursete pinnakattematerjalide arenduse tähtsust.

Artiklis III uuriti kulumise mõju ZnO osakesi sisaldavate akrüülsete pinnakatete fotokatalüütilistele omadustele roostevabast terasest alustel. Töö käigus viidi läbi kolme erinevat tüüpi pinnatötlused (märg, kuiv ja abrasiivne), et hinnata ZnO nanoosakesi ja kommertsiaalseid ZnO mikroosakesi sisaldavate akrüülsete pinnakatete vastupidavust simuleeritud kulumisele. SEM analüüs demonstreeris akrüülkatte siledat pinnastruktuuri enne töötlemist ning selgeid muutusi

pinnakatete abrasiivtöötlemise järel (jäljed, kriimud). Valmistatud akrüülipõhised nanokomposiitsed pinnad olid hüdrofoobsed ja jäid hüdrofoobseks ka pärast simuleeritud kulumist (kontaktnurk $> 90^\circ$). Kommertsiaalsete ja sünteesitud ZnO põhiste katete fotokatalüütiline efektiivsus pärast märg- ja kuivtöötlemist oli 6 h UVA ($2.5\text{--}3 \text{ W/m}^2$) eksponeerimise järel ligikaudu 10% hinnates MS lagunemise kaudu. Abrasiivne töötlemine suurendas MS lagunemiskiirust 25%-ni samasuguse UVA ekspositsiooni korral. Tulemused näitasid, et ZnO nanoosakestel ja kommertsiaalsel ZnO mikroosakestel põhinevad akrüülkatted säilitasid kulutava pinnatöötlemise järel fotokatalüütilise efektiivsuse ning see isegi suurenes abrasiivtöötlemise korral.

IV artikkel käesolevas väitekirjas analüüsib kommertsiaalseid TiO₂-põhiseid fotokatalüütilisi klaase, BIOCLEAN® ja SaniTise™. Seejuures SaniTise™ puhul on tootja turustanud seda antimikroobse aknaklaasina. Nende klaaspindade puhul tuvastati mõõdukas MS lagunemine (vastavalt 20% ja 40%) üle 72 h kestusega suure intensiivsusega UVA ekspositsiooni korral ($22\text{--}25 \text{ W/m}^2$). Pinna hüdrofiilsus suurenes UVA eeltöötlemise korral, esialgne vee kontaktnurk 60° vähenes pärast 24 h UVA-ga eksponeerimist $\leq 10^\circ$ -le. Klaaside pinnakatted kaotasid aga hüdrofiilsuse ilma jätkuva UVA ekspositsioonita. Käesoleva töö tulemused näitasid, et TiO₂-põhiste pindade fotokatalüütilise aktiivsuse muutus ja kontaktnurga meetodil määratud pinna fotoindutseeritud hüdrofiilsuse muutused ei langenud kokku. Peamine põhjus on see, et fotoergastuse mõjul toimub pinnal kaks erinevat protsessi. Fotokatalüüs hõlmab pinna aktiveerimist valguse abil, mille käigus algavad saasteaineid degradeerivad keemilised reaktsioonid. Fotoindutseeritud hüdrofiilsus aga suurendab pinna afiinsust vee suhtes, mille tulemusena vesi paikneb suuremale pinnale. Kokkuvõttes võib öelda, et SaniTise™ näitas suuremat fotokatalüütilist ja antibakteriaalset aktiivsust kui BIOCLEAN®, viimane oli ainult marginaalselt efektiivsem kui pinnakatteta kontrollklaas.

Käesolev doktoritöö hõlmab fotokatalüütiliste materjalide arenduse erinevaid aspekte ja aitas mõista nende koostise ja struktuuri mõju potentsiaalsele rakendatavusele. Uudsed ja innovatiivsed materjalide kombinatsioonid, nagu magnetiliselt kokkukogutav CuFe₂O₄-Fe₂O₃ koos TiO₂-P25-ga, võimaldavad suurendada fotokatalüütiliste materjalide funktsionaalsust ja rakendatavust. Uuringute tulemusena näidati, et nano-ZnO ja nano-ZnO/Ag osakestel põhinevate akrüülsete pinnakatete fotokatalüütiline aktiivsus oli sarnane kommertsiaalsele TiO₂-l põhinevale SaniTise™ klaasile. Samuti näitasid töö tulemused, et ZnO osakestel põhinevad akrüülkatted säilitavad fotokatalüütilise efektiivsuse pärast kulutatavat pinnatöötlust ja on seega potentsiaalselt kasutatavad.

Doktoritöö käigus olen mõistnud efektiivsete fotokatalüüsitorite ja fotokatalüüsil põhinevate antimikroobsete materjalide arendamise tähtsust. Seejuures on olulised innovaativsed materjalikombinatsioonid, põhjalik karakteriseerimine, sünteesi optimeerimine, materjalide efektiivsus ja ka vastupidavus. Kokkuvõttes näitavad käesoleva doktoritöö raames välja töötatud ja uuritud fotokatalüütilised materjalid suurt potentsiaali nii vee puhastamise kui ka antimikroobsete katete valmistamise jaoks.

ACKNOWLEDGEMENTS

First and foremost, I extend my deepest gratitude to my supervisors, Rainer Pärna, Vambola Kisand, and Angela Ivask, for their invaluable guidance, patience, and support throughout my PhD journey. I am profoundly proud and grateful to have had the opportunity to work under their mentorship.

I am deeply grateful to the colleagues from the X-ray spectroscopy laboratory, including Mati Kook, Arvo Tõnisoo, Tanel Käämbre, Juhan Matthias Kahk, and my Master's thesis supervisor, Arvo Kikas, for their contributions and support. A special acknowledgement goes to my office neighbor, Marta Berholts, and her husband, Artjom Berholts, for their friendship and encouragement.

I would like to extend my sincere gratitude to all my co-authors, whose collaborations have enriched the work included in this thesis. I am particularly thankful to Raivo Stern, Joosep Link from the National Institute of Chemical Physics and Biophysics in Tallinn, and Alexander Gogos from Empa St. Gallen for their valuable contributions.

My academic journey was significantly supported by various individuals and institutions during internships and visits to laboratories in Kajaani, Helsinki, Oulu, St Gallen, and Zurich. To all who enhanced my skills and expanded my understanding of science, thank you.

I am deeply grateful for the unwavering support of my family in Ukraine and my friends, who have been a constant source of encouragement throughout this journey.

Finally, my utmost gratitude goes to my beloved wife, Sevanna, for her incredible support, patience, and love. Her unwavering belief in me has been the driving force behind this accomplishment. Yes k'ez sirum yem!

REFERENCES

1. Gao W, Zhang L (2021) Nanomaterials arising amid antibiotic resistance. *Nat Rev Microbiol* 19:5–6. <https://doi.org/10.1038/s41579-020-00469-5>
2. Beni AA, Jabbari H (2022) Nanomaterials for Environmental Applications. *Results Eng* 15:100467. <https://doi.org/10.1016/j.rineng.2022.100467>
3. Rajasulochana P, Preethy V (2016) Comparison on efficiency of various techniques in treatment of waste and sewage water – A comprehensive review. *Resour-Effic Technol* 2:175–184. <https://doi.org/10.1016/j.reffit.2016.09.004>
4. Chong MN, Jin B, Chow CWK, Saint C (2010) Recent developments in photocatalytic water treatment technology: A review. *Water Res* 44:2997–3027. <https://doi.org/10.1016/j.watres.2010.02.039>
5. Rueda-Marquez JJ, Levchuk I, Ibañez PF, Sillanpää M (2020) A critical review on application of photocatalysis for toxicity reduction of real wastewaters. *J Clean Prod* 258:120694. <https://doi.org/10.1016/j.jclepro.2020.120694>
6. Koe WS, Lee JW, Chong WC, et al (2020) An overview of photocatalytic degradation: photocatalysts, mechanisms, and development of photocatalytic membrane. *Environ Sci Pollut R* 27:2522–2565. <https://doi.org/10.1007/s11356-019-07193-5>
7. Bhatkhande DS, Pangarkar VG, Beenackers AACM (2002) Photocatalytic degradation for environmental applications – a review. *J Chem Technol Biotechnol* 77: 102–116. <https://doi.org/10.1002/jctb.532>
8. Humayun M, Wang C, Luo W (2022) Recent Progress in the Synthesis and Applications of Composite Photocatalysts: A Critical Review. *Small Methods* 6:e2101395. <https://doi.org/10.1002/smt.202101395>
9. Anandan S, Ikuma Y, Niwa K (2010) An Overview of Semi-Conductor Photocatalysis: Modification of TiO₂ Nanomaterials. *Solid State Phenom* 162:239–260. <https://doi.org/10.4028/www.scientific.net/ssp.162.239>
10. Xu Z, Ren Y, Deng X, et al (2022) Recent Developments on Gas-Phase Volatile Organic Compounds Abatement Based on Photocatalysis. *Adv Energy Sustain Res* 3:. <https://doi.org/10.1002/aesr.202200105>
11. Gopinath KP, Madhav NV, Krishnan A, et al (2020) Present applications of titanium dioxide for the photocatalytic removal of pollutants from water: A review. *J Environ Manag* 270:110906. <https://doi.org/10.1016/j.jenvman.2020.110906>
12. Ren C, Yang B, Wu M, et al (2010) Synthesis of Ag/ZnO nanorods array with enhanced photocatalytic performance. *J Hazard Mater* 182:123–129. <https://doi.org/10.1016/j.jhazmat.2010.05.141>
13. Hernández-Alonso MD, Fresno F, Suárez S, Coronado JM (2009) Development of alternative photocatalysts to TiO₂: Challenges and opportunities. *Energy Environ Sci* 2:1231–1257. <https://doi.org/10.1039/b907933e>
14. Lu W, Liu G, Gao S, et al (2008) Tyrosine-assisted preparation of Ag/ZnO nanocomposites with enhanced photocatalytic performance and synergistic antibacterial activities. *Nanotechnology* 19:445711. <https://doi.org/10.1088/0957-4484/19/44/445711>
15. Rosenberg M, Visnapuu M, Saal K, et al (2021) Preparation and Characterization of Photocatalytically Active Antibacterial Surfaces Covered with Acrylic Matrix Embedded Nano-ZnO and Nano-ZnO/Ag. *Nanomater Basel Switz* 11:3384. <https://doi.org/10.3390/nano11123384>

16. Danilian D, Bundrűck FM, Kikas A, et al (2024) Reusable magnetic mixture of CuFe 2 O 4 –Fe 2 O 3 and TiO 2 for photocatalytic degradation of pesticides in water. *RSC Adv* 14:12337–12348. <https://doi.org/10.1039/d4ra00094c>
17. Gupta SM, Tripathi M (2011) A review of TiO2 nanoparticles. *Chin Sci Bull* 56: 1639. <https://doi.org/10.1007/s11434-011-4476-1>
18. Schneider J, Matsuoka M, Takeuchi M, et al (2014) Understanding TiO2 Photocatalysis: Mechanisms and Materials. *Chem Rev* 114:9919–9986. <https://doi.org/10.1021/cr5001892>
19. Guo Q, Zhou C, Ma Z, Yang X (2019) Fundamentals of TiO2 Photocatalysis: Concepts, Mechanisms, and Challenges. *Adv Mater* 31:e1901997. <https://doi.org/10.1002/adma.201901997>
20. Zhu S, Wang D (2017) Photocatalysis: Basic Principles, Diverse Forms of Implementations and Emerging Scientific Opportunities. *Adv Energy Mater* 7:. <https://doi.org/10.1002/aenm.201700841>
21. Hashimoto K, Irie H, Fujishima A (2005) TiO2 Photocatalysis: A Historical Overview and Future Prospects. *Jpn J Appl Phys* 44:8269. <https://doi.org/10.1143/jjap.44.8269>
22. Yadav HM, Kim J-S, Pawar SH (2016) Developments in photocatalytic antibacterial activity of nano TiO2: A review. *Korean J Chem Eng* 33:1989–1998. <https://doi.org/10.1007/s11814-016-0118-2>
23. Zhou Z, Li B, Liu X, et al (2021) Recent Progress in Photocatalytic Antibacterial. *ACS Appl Bio Mater* 4:3909–3936. <https://doi.org/10.1021/acsabm.0c01335>
24. Dong H, Zeng G, Tang L, et al (2015) An overview on limitations of TiO2-based particles for photocatalytic degradation of organic pollutants and the corresponding countermeasures. *Water Res* 79:128–146. <https://doi.org/10.1016/j.watres.2015.04.038>
25. Hanaor DAH, Sorrell CC (2011) Review of the anatase to rutile phase transformation. *J Mater Sci* 46:855–874. <https://doi.org/10.1007/s10853-010-5113-0>
26. Kisand V, Joost U, Reedo V, et al (2010) Influence of the heating temperature on the properties of nickel doped TiO2 films prepared by sol–gel method. *Appl Surf Sci* 256:4538–4542. <https://doi.org/10.1016/j.apsusc.2010.02.043>
27. Humayun M, Raziq F, Khan A, Luo W (2018) Modification strategies of TiO2 for potential applications in photocatalysis: a critical review. *Green Chem Lett Rev* 11:86–102. <https://doi.org/10.1080/17518253.2018.1440324>
28. Pereira L de O, Sales IM, Zampiere LP, et al (2019) Preparation of magnetic photocatalysts from TiO2, activated carbon and iron nitrate for environmental remediation. *J Photochem Photobiol A: Chem* 382:111907. <https://doi.org/10.1016/j.jphotochem.2019.111907>
29. Zielińska-Jurek A, Bielan Z, Wysocka I, et al (2017) Magnetic semiconductor photocatalysts for the degradation of recalcitrant chemicals from flow back water. *J Environ Manag* 195:157–165. <https://doi.org/10.1016/j.jenvman.2016.06.056>
30. Ong CB, Ng LY, Mohammad AW (2018) A review of ZnO nanoparticles as solar photocatalysts: Synthesis, mechanisms and applications. *Renew Sustain Energy Rev* 81:536–551. <https://doi.org/10.1016/j.rser.2017.08.020>
31. Kumar SG, Rao KSRK (2014) Zinc oxide based photocatalysis: tailoring surface-bulk structure and related interfacial charge carrier dynamics for better environmental applications. *RSC Adv* 5:3306–3351. <https://doi.org/10.1039/c4ra13299h>

32. Kumar Rajesh, Umar Ahmad, Kumar Girish, Nalwa HS (2017) Antimicrobial properties of ZnO nanomaterials: A review. *Ceram Int* 43:3940–3961. <https://doi.org/10.1016/j.ceramint.2016.12.062>
33. Sirelkhatim A, Mahmud S, Seeni A, et al (2015) Review on Zinc Oxide Nanoparticles: Antibacterial Activity and Toxicity Mechanism. *Nano-Micro Lett* 7:219–242. <https://doi.org/10.1007/s40820-015-0040-x>
34. Deshpande RA, Navne J, Adelmark MV, et al (2024) Understanding the light induced hydrophilicity of metal-oxide thin films. *Nat Commun* 15:124. <https://doi.org/10.1038/s41467-023-44603-2>
35. Wang R, Hashimoto K, Fujishima A, et al (1998) Photogeneration of Highly Amphiphilic TiO₂ Surfaces. *Adv Mater* 10:135–138. [https://doi.org/10.1002/\(sici\)1521-4095\(199801\)10:2<135::aid-adma135>3.0.co;2-m](https://doi.org/10.1002/(sici)1521-4095(199801)10:2<135::aid-adma135>3.0.co;2-m)
36. Banerjee S, Dionysiou DD, Pillai SC (2015) Self-cleaning applications of TiO₂ by photo-induced hydrophilicity and photocatalysis. *Appl Catal B: Environ* 176:396–428. <https://doi.org/10.1016/j.apcatb.2015.03.058>
37. Bolis V, Busco C, Ciarletta M, et al (2012) Hydrophilic/hydrophobic features of TiO₂ nanoparticles as a function of crystal phase, surface area and coating, in relation to their potential toxicity in peripheral nervous system. *J Colloid Interface Sci* 369:28–39. <https://doi.org/10.1016/j.jcis.2011.11.058>
38. Cwikel D, Zhao Q, Liu C, et al (2010) Comparing Contact Angle Measurements and Surface Tension Assessments of Solid Surfaces. *Langmuir* 26:15289–15294. <https://doi.org/10.1021/la1020252>
39. Wong MS, Nakamura S, DenBaars SP (2021) High external quantum efficiency III-nitride micro-light-emitting diodes. *Semicond Semimet* 95–121. <https://doi.org/10.1016/bs.semsem.2020.12.005>
40. Tempelaar R, Koster LJA, Havenith RWA, et al (2016) Charge Recombination Suppressed by Destructive Quantum Interference in Heterojunction Materials. *J Phys Chem Lett* 7:198–203. <https://doi.org/10.1021/acs.jpcclett.5b02580>
41. Marina PF, Cheng C, Sedev R, et al (2018) Van der Waals Emulsions: Emulsions Stabilized by Surface-Inactive, Hydrophilic Particles via van der Waals Attraction. *Angew Chem Int Ed* 57:9510–9514. <https://doi.org/10.1002/anie.201805410>
42. Carp O, Huisman CL, Reller A (2004) Photoinduced reactivity of titanium dioxide. *Prog Solid State Chem* 32:33–177. <https://doi.org/10.1016/j.progsolidstchem.2004.08.001>
43. Balasubramaniam B, Prateek, Ranjan S, et al (2021) Antibacterial and Antiviral Functional Materials: Chemistry and Biological Activity toward Tackling COVID-19-like Pandemics. *ACS Pharmacol Transl Sci* 4:8–54. <https://doi.org/10.1021/acspsci.0c00174>
44. Cassidy SS, Sanders DJ, Wade J, et al (2020) Antimicrobial surfaces: A need for stewardship? *Plos Pathog* 16:e1008880. <https://doi.org/10.1371/journal.ppat.1008880>
45. Swartjes JJTM, Sharma PK, Kooten TG, et al (2015) Current Developments in Antimicrobial Surface Coatings for Biomedical Applications. *Curr Med Chem* 22:2116–2129. <https://doi.org/10.2174/0929867321666140916121355>
46. Salgado CD, Sepkowitz KA, John JF, et al (2013) Copper surfaces reduce the rate of healthcare-acquired infections in the intensive care unit. *Infect Cont Hosp Ep* 34:479–86. <https://doi.org/10.1086/670207>

47. Casey AL, Adams D, Karpanen TJ, et al (2010) Role of copper in reducing hospital environment contamination. *J Hosp Infect* 74:72–77. <https://doi.org/10.1016/j.jhin.2009.08.018>
48. Mikolay A, Huggett S, Tikana L, et al (2010) Survival of bacteria on metallic copper surfaces in a hospital trial. *Appl Microbiol Biot* 87:1875–9. <https://doi.org/10.1007/s00253-010-2640-1>
49. Burke GH, Butler JP (2018) Analysis of the role of copper impregnated composite hard surfaces, bed linens and patient gowns in reducing healthcare-associated infection rates. *Int J Infect Control* 14:. <https://doi.org/10.3396/ijic.v14i1.005.18>
50. Michels HT, Anderson DG (2008) Antimicrobial regulatory efficacy testing of solid copper alloy surfaces in the USA. *Metal Ions in Biology and Medicine* 10:185–190
51. Gomes IB, Simões M, Simões LC (2020) Copper Surfaces in Biofilm Control. *Nanomaterials-basel* 10:2491. <https://doi.org/10.3390/nano10122491>
52. Joost U, Juganson K, Visnapuu M, et al (2015) Photocatalytic antibacterial activity of nano-TiO₂ (anatase)-based thin films: Effects on *Escherichia coli* cells and fatty acids. *J Photochem Photobiology B Biology* 142:178–185. <https://doi.org/10.1016/j.jphotobiol.2014.12.010>
53. Joost U, Pärna R, Lembinen M, et al (2013) Heat treatment and substrate dependant properties of titania thin films with high copper loading. *Phys Status Solidi A* 210:1201–1212. <https://doi.org/10.1002/pssa.201228751>
54. Carvalho TB de, Barbosa JB, Teixeira P (2024) Assessing Antimicrobial Efficacy on Plastics and Other Non-Porous Surfaces: A Closer Look at Studies Using the ISO 22196:2011 Standard. *Biology* 13:59. <https://doi.org/10.3390/biology13010059>
55. Cunliffe AJ, Askew PD, Stephan I, et al (2021) How Do We Determine the Efficacy of an Antibacterial Surface? A Review of Standardised Antibacterial Material Testing Methods. *Antibiotics* 10:1069. <https://doi.org/10.3390/antibiotics10091069>
56. Mahanta U, Khandelwal M, Deshpande AS (2021) Antimicrobial surfaces: a review of synthetic approaches, applicability and outlook. *J Mater Sci* 56:17915–17941. <https://doi.org/10.1007/s10853-021-06404-0>
57. Vatansever F, Melo WCMA de, Avci P, et al (2013) Antimicrobial strategies centered around reactive oxygen species – bactericidal antibiotics, photodynamic therapy, and beyond. *Fems Microbiol Rev* 37:955–989. <https://doi.org/10.1111/1574-6976.12026>
58. Hasan J, Crawford RJ, Ivanova EP (2013) Antibacterial surfaces: the quest for a new generation of biomaterials. *Trends Biotechnol* 31:295–304. <https://doi.org/10.1016/j.tibtech.2013.01.017>
59. LI D, QU J (2009) The progress of catalytic technologies in water purification: A review. *J Environ Sci* 21:713–719. [https://doi.org/10.1016/s1001-0742\(08\)62329-3](https://doi.org/10.1016/s1001-0742(08)62329-3)
60. Kesari KK, Soni R, Jamal QMS, et al (2021) Wastewater Treatment and Reuse: a Review of its Applications and Health Implications. *Water, Air, Soil Pollut* 232:208. <https://doi.org/10.1007/s11270-021-05154-8>
61. Syafrudin M, Kristanti RA, Yuniarto A, et al (2021) Pesticides in Drinking Water – A Review. *Int J Environ Res Public Heal* 18:468. <https://doi.org/10.3390/ijerph18020468>
62. Marsala RZ, Capri E, Russo E, et al (2020) First evaluation of pesticides occurrence in groundwater of Tidone Valley, an area with intensive viticulture. *Sci Total Environ* 736:139730. <https://doi.org/10.1016/j.scitotenv.2020.139730>

63. Gilca AF, Teodosiu C, Fiore S, Musteret CP (2020) Emerging disinfection byproducts: A review on their occurrence and control in drinking water treatment processes. *Chemosphere* 259:127476. <https://doi.org/10.1016/j.chemosphere.2020.127476>
64. Gupta VK, Ali I (2013) *Environmental Water*. 1–27. <https://doi.org/10.1016/b978-0-444-59399-3.00001-5>
65. Ren G, Han H, Wang Y, et al (2021) Recent Advances of Photocatalytic Application in Water Treatment: A Review. *Nanomaterials-basel* 11:1804. <https://doi.org/10.3390/nano11071804>
66. He H, Luo Z, Yu C (2020) Diatomite-anchored g-C₃N₄ nanosheets for selective removal of organic dyes. *J Alloy Compd* 816:152652. <https://doi.org/10.1016/j.jallcom.2019.152652>
67. He H, Luo Z, Yu C (2021) Embellish zinc tungstate nanorods with silver chloride nanoparticles for enhanced photocatalytic, antibacterial and antifouling performance. *Colloids Surf A: Physicochem Eng Asp* 613:126099. <https://doi.org/10.1016/j.colsurfa.2020.126099>
68. He H, Luo Z, Tang Z-Y, Yu C (2019) Controllable construction of ZnWO₄ nanostructure with enhanced performance for photosensitized Cr(VI) reduction. *Appl Surf Sci* 490:460–468. <https://doi.org/10.1016/j.apsusc.2019.05.260>
69. Yi F, Ma J, Lin C, et al (2022) Electronic and thermal transfer actuating memory catalysis for organic removal by a plasmonic photocatalyst. *Chem Eng J* 427:132028. <https://doi.org/10.1016/j.cej.2021.132028>
70. Mishra M, Chun D-M (2015) α -Fe₂O₃ as a photocatalytic material: A review. *Appl Catal A: Gen* 498:126–141. <https://doi.org/10.1016/j.apcata.2015.03.023>
71. Cornell DrRM, Schwertmann Prof em. DrDr h. c. U (2003) *The Iron Oxides*
72. Kumar MRA, Abebe B, Nagaswarupa HP, et al (2020) Enhanced photocatalytic and electrochemical performance of TiO₂-Fe₂O₃ nanocomposite: Its applications in dye decolorization and as supercapacitors. *Sci Rep* 10:1249. <https://doi.org/10.1038/s41598-020-58110-7>
73. Bootluck W, Chittrakarn T, Techato K, Khongnakorn W (2021) Modification of surface α -Fe₂O₃/TiO₂ photocatalyst nanocomposite with enhanced photocatalytic activity by Ar gas plasma treatment for hydrogen evolution. *J Environ Chem Eng* 9: 105660. <https://doi.org/10.1016/j.jece.2021.105660>
74. Yadav RS, Havlica J, Masilko J, et al (2016) Cation Migration-Induced Crystal Phase Transformation in Copper Ferrite Nanoparticles and Their Magnetic Property. *J Supercond Nov Magn* 29:759–769. <https://doi.org/10.1007/s10948-015-3339-4>
75. Yi F, Ma J, Lin C, et al (2020) Insights into the enhanced adsorption/photocatalysis mechanism of a Bi₄O₅Br₂/g-C₃N₄ nanosheet. *J Alloy Compd* 821:153557. <https://doi.org/10.1016/j.jallcom.2019.153557>
76. He H, Jiang J, Luo Z, et al (2023) Novel starfish-like inorganic/organic heterojunction for Cr(VI) photocatalytic reduction in neutral solution. *Colloids Surf A: Physicochem Eng Asp* 667:131357. <https://doi.org/10.1016/j.colsurfa.2023.131357>
77. Gong Y-N, Mei J-H, Liu J-W, et al (2021) Manipulating metal oxidation state over ultrastable metal-organic frameworks for boosting photocatalysis. *Appl Catal B: Environ* 292:120156. <https://doi.org/10.1016/j.apcatb.2021.120156>
78. Lam SW, Hermawan M, Coleman HM, et al (2007) The role of copper(II) ions in the photocatalytic oxidation of 1,4-dioxane. *J Mol Catal A: Chem* 278:152–159. <https://doi.org/10.1016/j.molcata.2007.09.007>

79. Gharaei SK, Abbasnejad M, Maezono R (2018) Bandgap reduction of photocatalytic TiO₂ nanotube by Cu doping. *Sci Rep* 8:14192. <https://doi.org/10.1038/s41598-018-32130-w>
80. Watts JF, Wolstenholme J (2024) An Introduction to Surface Analysis by XPS and AES. <https://doi.org/10.1002/9781119417651>
81. Greczynski G, Hultman L (2020) X-ray photoelectron spectroscopy: Towards reliable binding energy referencing. *Prog Mater Sci* 107:100591. <https://doi.org/10.1016/j.pmatsci.2019.100591>
82. Krishna DNG, Philip J (2022) Review on surface-characterization applications of X-ray photoelectron spectroscopy (XPS): Recent developments and challenges. *Appl Surf Sci Adv* 12:100332. <https://doi.org/10.1016/j.apsadv.2022.100332>
83. Makuła P, Pacia M, Macyk W (2018) How To Correctly Determine the Band Gap Energy of Modified Semiconductor Photocatalysts Based on UV–Vis Spectra. *J Phys Chem Lett* 9:6814–6817. <https://doi.org/10.1021/acs.jpcllett.8b02892>
84. Swinehart DF (1962) The Beer-Lambert Law. *J Chem Educ* 39:333. <https://doi.org/10.1021/ed039p333>
85. Tissue BM (2013) Characterization of Materials. 1–13. <https://doi.org/10.1002/0471266965.com059.pub2>
86. Ameh ES (2019) A review of basic crystallography and x-ray diffraction applications. *Int J Adv Manuf Technol* 105:3289–3302. <https://doi.org/10.1007/s00170-019-04508-1>
87. (2014) Practical Materials Characterization. <https://doi.org/10.1007/978-1-4614-9281-8>
88. Watanabe M (2010) Scanning Transmission Electron Microscopy, Imaging and Analysis. 291–351. https://doi.org/10.1007/978-1-4419-7200-2_7
89. Newbury* DE, Ritchie NWM (2013) Is Scanning Electron Microscopy/Energy Dispersive X-ray Spectrometry (SEM/EDS) Quantitative? *Scanning* 35:141–168. <https://doi.org/10.1002/sca.21041>
90. (2020) Antimicrobial Testing Methods & Procedures: Interim Method for Evaluating the Efficacy of Antimicrobial Surface Coatings
91. Sutar RS, Kalel PJ, Latthe SS, et al (2020) Superhydrophobic PVC/SiO₂ Coating for Self-Cleaning Application. *Macromol Symp* 393. <https://doi.org/10.1002/masy.202000034>
92. RepRap. reprap.org
93. Peruchon L, Puzenat E, Girard-Egrot A, et al (2008) Characterization of self-cleaning glasses using Langmuir–Blodgett technique to control thickness of stearic acid multilayers Importance of spectral emission to define standard test. *J Photochem Photobiol A: Chem* 197:170–176. <https://doi.org/10.1016/j.jphotochem.2007.12.033>
94. Fairley N, Fernandez V, Richard-Plouet M, et al (2021) Systematic and collaborative approach to problem solving using X-ray photoelectron spectroscopy. *Appl Surf Sci Adv* 5:100112. <https://doi.org/10.1016/j.apsadv.2021.100112>
95. Kumar M, Islam MN, Terry FL, et al (2012) Stand-off detection of solid targets with diffuse reflection spectroscopy using a high-power mid-infrared supercontinuum source. *Appl Opt* 51:2794. <https://doi.org/10.1364/ao.51.002794>
96. Oss CJ van (1993) Acid – base interfacial interactions in aqueous media. *Colloids Surfaces Physicochem Eng Aspects* 78:1–49. [https://doi.org/10.1016/0927-7757\(93\)80308-2](https://doi.org/10.1016/0927-7757(93)80308-2)

97. Schneider CA, Rasband WS, Eliceiri KW (2012) NIH Image to ImageJ: 25 years of image analysis. *Nat Methods* 9:671–675. <https://doi.org/10.1038/nmeth.2089>
98. Law K-Y (2014) Definitions for Hydrophilicity, Hydrophobicity, and Superhydrophobicity: Getting the Basics Right. *J Phys Chem Lett* 5:686–688. <https://doi.org/10.1021/jz402762h>
99. Pärna R, Sankari R, Kukk E, et al (2017) FinEstBeAMS – A wide-range Finnish-Estonian Beamline for Materials Science at the 1.5GeV storage ring at the MAX IV Laboratory. *Nucl Instrum Methods Phys Res Sect A: Accel, Spectrometers, Detect Assoc Equip* 859:83–89. <https://doi.org/10.1016/j.nima.2017.04.002>
100. Wang W, Kivimäki A, Chernenko K, et al (2022) A new user-friendly materials science end station at the FinEstBeAMS beamline of MAX IV. *J Phys: Conf Ser* 2380:012048. <https://doi.org/10.1088/1742-6596/2380/1/012048>
101. QD Application Note 1500-021 Rev. B0 (07/2020)
102. Ohno T, Sarukawa K, Tokieda K, Matsumura M (2001) Morphology of a TiO₂ Photocatalyst (Degussa, P-25) Consisting of Anatase and Rutile Crystalline Phases. *J Catal* 203:82–86. <https://doi.org/10.1006/jcat.2001.3316>
103. Golshan M, Kakavandi B, Ahmadi M, Azizi M (2018) Photocatalytic activation of peroxymonosulfate by TiO₂ anchored on copper ferrite (TiO₂@CuFe₂O₄) into 2,4-D degradation: Process feasibility, mechanism and pathway. *J Hazard Mater* 359: 325–337. <https://doi.org/10.1016/j.jhazmat.2018.06.069>
104. Toby BH (2006) R factors in Rietveld analysis: How good is good enough? *Powder Diffr* 21:67–70. <https://doi.org/10.1154/1.2179804>
105. McCafferty E, Wightman JP (1998) Determination of the concentration of surface hydroxyl groups on metal oxide films by a quantitative XPS method. *Surf Interface Anal* 26:549–564. [https://doi.org/10.1002/\(sici\)1096-9918\(199807\)26:8<549::aid-sia396>3.0.co;2-q](https://doi.org/10.1002/(sici)1096-9918(199807)26:8<549::aid-sia396>3.0.co;2-q)
106. Yeh JJ, Lindau I (1985) Atomic subshell photoionization cross sections and asymmetry parameters: $1 \leq Z \leq 103$. *At Data Nucl Data Tables* 32:1–155. [https://doi.org/10.1016/0092-640x\(85\)90016-6](https://doi.org/10.1016/0092-640x(85)90016-6)
107. Yamashita T, Hayes P (2008) Analysis of XPS spectra of Fe²⁺ and Fe³⁺ ions in oxide materials. *Appl Surf Sci* 254:2441–2449. <https://doi.org/10.1016/j.apsusc.2007.09.063>
108. Qin Q, Liu Y, Li X, et al (2018) Enhanced heterogeneous Fenton-like degradation of methylene blue by reduced CuFe₂O₄. *RSC Adv* 8:1071–1077. <https://doi.org/10.1039/c7ra12488k>
109. He H, Xiao J, Liu Z, et al (2023) Boosting the hydrogen evolution of layered double hydroxide by optimizing the electronic structure and accelerating the water dissociation kinetics. *Chem Eng J* 453:139751. <https://doi.org/10.1016/j.cej.2022.139751>
110. Moulder JF, Stickle WF, Sobol PE, Bomben KD (1992) *Handbook of X-ray Photoelectron Spectroscopy*. Eden Prairie: Perkin-Elmer Corporation
111. Laan G van der, Westra C, Haas C, Sawatzky GA (1981) Satellite structure in photoelectron and Auger spectra of copper dihalides. *Phys Rev B* 23:4369–4380. <https://doi.org/10.1103/physrevb.23.4369>
112. He H, Zeng L, Peng X, et al (2023) Porous cobalt sulfide nanosheets arrays with low valence copper incorporated for boosting alkaline hydrogen evolution via lattice engineering. *Chem Eng J* 451:138628. <https://doi.org/10.1016/j.cej.2022.138628>

113. Li Z, Lyu J, Ge M (2018) Synthesis of magnetic Cu/CuFe₂O₄ nanocomposite as a highly efficient Fenton-like catalyst for methylene blue degradation. *J Mater Sci* 53:15081–15095. <https://doi.org/10.1007/s10853-018-2699-0>
114. Wang X, Pehkonen SO, Rämö J, et al (2011) Experimental and computational studies of nitrogen doped Degussa P25 TiO₂: application to visible-light driven photo-oxidation of As(III). *Catal Sci Technol* 2:784–793. <https://doi.org/10.1039/c2cy00486k>
115. Piccinin S (2019) The band structure and optical absorption of hematite (α -Fe₂O₃): a first-principles GW-BSE study. *Phys Chem Chem Phys* 21:2957–2967. <https://doi.org/10.1039/c8cp07132b>
116. Xia C, Jia Y, Tao M, Zhang Q (2013) Tuning the band gap of hematite α -Fe₂O₃ by sulfur doping. *Phys Lett A* 377:1943–1947. <https://doi.org/10.1016/j.physleta.2013.05.026>
117. Li W, Wu H (2017) Sodium citrate functionalized reusable Fe₃O₄@TiO₂ photocatalyst for water purification. *Chem Phys Lett* 686:178–182. <https://doi.org/10.1016/j.cplett.2017.08.046>
118. Ni Y, Wang M, Liu L, et al (2022) Efficient and reusable photocatalytic river water disinfection by additive graphitic carbon nitride/magnesium oxide nano-onions with particular “nano-magnifying glass effect.” *J Hazard Mater* 439:129533. <https://doi.org/10.1016/j.jhazmat.2022.129533>
119. Magill SS, Edwards JR, Bamberg W, et al (2014) Multistate Point-Prevalence Survey of Health Care–Associated Infections. *N Engl J Med* 370:1198–1208. <https://doi.org/10.1056/nejmoa1306801>
120. Sebastian D, Yao C-W, Lian I (2018) Mechanical Durability of Engineered Superhydrophobic Surfaces for Anti-Corrosion. *Coatings* 8:162. <https://doi.org/10.3390/coatings8050162>
121. Arulvel S, Reddy DM, Rufuss DDW, Akinaga T (2021) A comprehensive review on mechanical and surface characteristics of composites reinforced with coated fibres. *Surf Interfaces* 27:101449. <https://doi.org/10.1016/j.surfint.2021.101449>
122. Cui J, Shao Y, Zhang H, et al (2021) Development of a novel silver ions-nanosilver complementary composite as antimicrobial additive for powder coating. *Chem Eng J* 420:127633. <https://doi.org/10.1016/j.cej.2020.127633>
123. Liu G, Wu G, Jin C, Kong Z (2015) Preparation and antimicrobial activity of terpene-based polyurethane coatings with carbamate group-containing quaternary ammonium salts. *Prog Org Coat* 80:150–155. <https://doi.org/10.1016/j.porgcoat.2014.12.005>
124. Calovi M, Coroneo V, Palanti S, Rossi S (2023) Colloidal silver as innovative multifunctional pigment: The effect of Ag concentration on the durability and biocidal activity of wood paints. *Prog Org Coat* 175:107354. <https://doi.org/10.1016/j.porgcoat.2022.107354>
125. Hochmannova L, Vytrasova J (2010) Photocatalytic and antimicrobial effects of interior paints. *Prog Org Coat* 67:1–5. <https://doi.org/10.1016/j.porgcoat.2009.09.016>
126. Vu TV, Nguyen TV, Tabish M, et al (2021) Water-Borne ZnO/Acrylic Nanocoating: Fabrication, Characterization, and Properties. *Polymers* 13:717. <https://doi.org/10.3390/polym13050717>
127. Padmanabhan NT, John H (2020) Titanium dioxide based self-cleaning smart surfaces: A short review. *J Environ Chem Eng* 8:104211. <https://doi.org/10.1016/j.jece.2020.104211>

128. 'World's first' antimicrobial glass set to launch with third-party verification. <https://www.the-glazine.com/?p=1214>. Accessed 27 Oct 2020
129. (2010) SO 10678:2010; Fine Ceramics (Advanced Ceramics, Advanced Technical Ceramics) – Determination of Photocatalytic Activity of Surfaces in an Aqueous Medium by Degradation of Methylene Blue. International Organization for Standardization:
130. Guan K (2005) Relationship between photocatalytic activity, hydrophilicity and self-cleaning effect of TiO₂/SiO₂ films. *Surf Coat Technol* 191:155–160. <https://doi.org/10.1016/j.surfcoat.2004.02.022>

PUBLICATIONS

CURRICULUM VITAE

Name: Dmytro Danilian
Date of birth: 24.05.1996
Nationality: Ukranian
E-mail: dmytro.danilian@ut.ee

Education:

2020– ... University of Tartu, Faculty of Science and Technology, Institute of Physics, PhD student in Materials Science
2018–2020 University of Tartu, Faculty of Science and Technology, Institute of Chemistry, Master of Science (Applied Measurement Science)
2013–2018 National Technical University of Ukraine “Igor Sikorsky Kyiv Polytechnic Institute” (Kyiv, Ukraine), Faculty of Biomedical Engineering, Bachelor degree in Instrument Engineering
2018 Erasmus+ student in West Pomeranian University of Technology (Szczecin, Poland), Faculty of Electrical Engineering .
2009–2013 Lyceum of Informational Technology (Dnipro, Ukraine)
2006–2009 School no. 71 (Dnipro, Ukraine)
2003–2006 School no. 292 (Dnipro, Ukraine)

Career:

2022–... Junior research fellow at the University of Tartu (Estonia), Institute of Physics.
2022 Visiting PhD student, internship at the ETH Zurich and Swiss Federal Laboratories for Materials Science and Technology (St. Gallen, Switzerland), Nanoparticle Systems Engineering group.
2021 Visiting PhD student, internship at the University of Oulu (Finland), Nano and Molecular Systems Research Unit (NANOMO).
2020 Visiting researcher, internship at the University of Helsinki (Finland), Accelerator laboratory.
2019 Internship at the Kajaani University of Applied Sciences (Finland).
2017 Assistant engineer, internship at the Amosov National Institute of Cardiovascular Surgery (Kyiv, Ukraine), Department of Clinical Immunology.

Professional training:

2023 R C International Summer School 2023, Cutting Edge Neutron and X-ray Research for a Sustainable Future (L neburg, Germany).
2023 Estonian language summer school, A2>B1, University of Tartu, Estonia.
2023 Erasmus Blended Mobility “Spring School Self-Organization and Nanolithography”, Paderborn, Germany

- 2021 Baltic University Programme 8th PhD Students Training Interdisciplinary–Multicultural–International (Łódź, Poland).
- 2019 Eurachem workshop “Validation of targeted and non-targeted methods of Analysis”, Tartu, Estonia.

List of publications:

- Danilian, D.**; Bundrück, F. M.; Kikas, A.; Käämbre, T.; Mändar, H.; Gogos, A.; Kiisk, V.; Link, J.; Stern, R.; Ivask, A.; Kisand, V.; Pärna, R. Reusable magnetic mixture of $\text{CuFe}_2\text{O}_4\text{-Fe}_2\text{O}_3$ and TiO_2 for photocatalytic degradation of pesticides in water. *RSC Advances* **2024**, 14, 12337–12348, <https://doi.org/10.1039/D4RA00094C>
- Kook, M.; Kaur, H.; **Danilian, D.**; Rosenberg, M.; Kisand, V.; Ivask, A. Durability of Photocatalytic ZnO-Based Surface Coatings and Preservation of Their Antibacterial Effect after Simulated Wear. *J. Coat. Technol. Res.* **2024**, 1–12, <https://doi.org/10.1007/s11998-023-00868-2>.
- Kaur, H.; Rosenberg, M.; Kook, M.; **Danilian, D.**; Kisand, V.; Ivask, A. Antibacterial Activity of Solid Surfaces Is Critically Dependent on Relative Humidity, Inoculum Volume, and Organic Soiling. *FEMS Microbes* **2023**, 5, xtad022, <https://doi.org/10.1093/femsmc/xtad022>.
- Kisand, V.; Visnapuu, M.; Rosenberg, M.; **Danilian, D.**; Vlassov, S.; Kook, M.; Lange, S.; Pärna, R.; Ivask, A. Antimicrobial Activity of Commercial Photocatalytic SaniTise™ Window Glass. *Catalysts* **2022**, 12 (2), 197. <https://doi.org/10.3390/catal12020197>.
- Rosenberg, M.; Visnapuu, M.; Saal, K.; **Danilian, D.**; Pärna, R.; Ivask, A.; Kisand, V. Preparation and Characterization of Photocatalytically Active Antibacterial Surfaces Covered with Acrylic Matrix Embedded Nano-ZnO and Nano-ZnO/Ag. *Nanomater Basel Switz* **2021**, 11 (12), 3384. <https://doi.org/10.3390/nano11123384>.
- Kisand, K.; Sarapuu, A.; **Danilian, D.**; Kikas, A.; Kisand, V.; Rähn, M.; Treshchalov, A.; Käärik, M.; Merisalu, M.; Paiste, P.; Aruväli, J.; Leis, J.; Sammelselg, V.; Holdcroft, S.; Tammeveski, K. Transition Metal-Containing Nitrogen-Doped Nanocarbon Catalysts Derived from 5-Methylresorcinol for Anion Exchange Membrane Fuel Cell Application. *Journal of Colloid and Interface Science* **2021**, 584, 263–274. <https://doi.org/10.1016/j.jcis.2020.09.114>.

ELULOOKIRJELDUS

Nimi: Dmytro Danilian
Sünniaeg: 24.05.1996
Rahvus: Ukranian
E-post: dmytro.danilian@ut.ee

Haridus:

2020– ... Tartu Ülikool, Loodus- ja täppisteaduste valdkond, Füüsika-instituut, doktorant materjaliteaduses
2018–2020 Tartu Ülikool, Loodus- ja täppisteaduste valdkond, Keemia-instituut, rakendusmõõdeteaduse magister
2013–2018 Ukraina Riiklik Tehnikaülikool “Igor Sikorsky Kiievi Polütehniline Instituut” (Kiiev, Ukraina), biomeditsiinitehnika teaduskond, instrumentaaltehnika bakalaureusekraad
2018 Erasmus+ üliõpilane Lääne-Pommeri Tehnikaülikoolis (Szczecin, Poola), elektrotehnika teaduskond
2009–2013 Infotehnoloogia Lütseum (Dnipro, Ukraina)
2006–2009 Kool nr 71 (Dnipro, Ukraina)
2003–2006 Kool nr 292 (Dnipro, Ukraina)

Töökogemus:

2022–... Nooremteadur Tartu Ülikoolis (Eesti), Füüsikainstituut
2022 Külastav doktorant, internatuur ETH Zürichis ja Šveitsi Materjali-teaduse ja Tehnoloogia Föderaalsetes Laborites (St. Gallen, Šveits), Nanopartiklite Süsteemide Tehnika rühm
2021 Külastav doktorant, internatuur Oulu Ülikoolis (Soome), Nano- ja Molekulaarsüsteemide Uurimisüksus (NANOMO).
2020 Külastav teadur, internatuur Helsingi Ülikoolis (Soome), Kiirendi-labor.
2019 Praktika Kajaani Rakenduskõrgkoolis (Soome).
2017 Abiinsener, praktika Amosovi Rahvuslikus Kardiovaskulaar-kirurgia Instituudis (Kiiev, Ukraina), Kliinilise Immunoloogia Osakond.

Erialane täiendkoolitus:

2023 RÄC Rahvusvaheline Suvekool 2023, Lõikavate servade neutroni- ja röntgenuuringud jätkusuutliku tuleviku jaoks (Lüneburg, Saksamaa).
2023 Estonian language summer school, A2>B1, University of Tartu, Estonia.
2023 Erasmuse segamobiilsus “Kevadkool Eneseorganiseerumine ja Nanolitograafia”, Paderborn, Saksamaa

- 2021 Balti Ülikooli Programmi 8. doktorantide koolitus Interdistsiplinaarne–Multikultuurne–Rahvusvaheline (Łódź, Poola).
- 2019 Eurachem workshop „Sihtmääratud ja mittesihtmääratud meetodite valideerimine”, Tartu, Eesti

Publikatsioonide loetelu:

- Danilian, D.;** Bundrück, F. M.; Kikas, A.; Käämbre, T.; Mändar, H.; Gogos, A.; Kiisk, V.; Link, J.; Stern, R.; Ivask, A.; Kisand, V.; Pärna, R. Reusable magnetic mixture of $\text{CuFe}_2\text{O}_4\text{-Fe}_2\text{O}_3$ and TiO_2 for photocatalytic degradation of pesticides in water. *RSC Advances* 2024, 14, 12337–12348, <https://doi.org/10.1039/D4RA00094C>
- Kook, M.; Kaur, H.; **Danilian, D.;** Rosenberg, M.; Kisand, V.; Ivask, A. Durability of Photocatalytic ZnO-Based Surface Coatings and Preservation of Their Antibacterial Effect after Simulated Wear. *J. Coat. Technol. Res.* 2024, 1–12, doi:10.1007/s11998-023-00868-2.
- Kaur, H.; Rosenberg, M.; Kook, M.; **Danilian, D.;** Kisand, V.; Ivask, A. Antibacterial Activity of Solid Surfaces Is Critically Dependent on Relative Humidity, Inoculum Volume, and Organic Soiling. *FEMS Microbes* 2023, 5, xtad022, doi:10.1093/femsmc/xtad022.
- Kisand, V.; Visnapuu, M.; Rosenberg, M.; **Danilian, D.;** Vlassov, S.; Kook, M.; Lange, S.; Pärna, R.; Ivask, A. Antimicrobial Activity of Commercial Photocatalytic SaniTise™ Window Glass. *Catalysts* 2022, 12 (2), 197. <https://doi.org/10.3390/catal12020197>.
- Rosenberg, M.; Visnapuu, M.; Saal, K.; **Danilian, D.;** Pärna, R.; Ivask, A.; Kisand, V. Preparation and Characterization of Photocatalytically Active Antibacterial Surfaces Covered with Acrylic Matrix Embedded Nano-ZnO and Nano-ZnO/Ag. *Nanomater Basel Switz* 2021, 11 (12), 3384. <https://doi.org/10.3390/nano11123384>.
- Kisand, K.; Sarapuu, A.; **Danilian, D.;** Kikas, A.; Kisand, V.; Rähn, M.; Treshchalov, A.; Käärik, M.; Merisalu, M.; Paiste, P.; Aruväli, J.; Leis, J.; Sammelseig, V.; Holdcroft, S.; Tammeveski, K. Transition Metal-Containing Nitrogen-Doped Nanocarbon Catalysts Derived from 5-Methylresorcinol for Anion Exchange Membrane Fuel Cell Application. *Journal of Colloid and Interface Science* 2021, 584, 263–274. <https://doi.org/10.1016/j.jcis.2020.09.114>.

DISSERTATIONES SCIENTIAE MATERIALIS UNIVERSITATIS TARTUENSIS

1. **Martin Järvekülg.** Tubular microstructures by Hf-, Zr- and Ti-butoxide gel sheet rolling. Tartu, 2011, 112 p.
2. **Sergei Vlassov.** Investigation of nanoscale interactions and mechanical properties of nanostructures using quartz tuning fork based real-time measurements. Tartu, 2011, 171 p.
3. **Margus Kodu.** Pulsed Laser Deposition of Magnesium Oxide and Barium Ternary Oxides for Plasma Display Protective Layers. Tartu, 2011, 89 p.
4. **Rainer Pärna.** Surface studies of some oxide films. Tartu, 2011, 129 p.
5. **Jevgeni Šulga.** Self-assembly and interaction of nanostructures. Tartu, 2011, 114 p.
6. **Wojciech Kuznik.** Quantum-chemical computer simulations of the linear and non-linear optical properties of pyrazoloquinoline and dicyanopyrazine derivatives. Tartu, 2012, 89 p.
7. **Leonid Dorogin.** Structural and tribological properties of zero- and one-dimensional nanocrystals. Tartu, 2012, 193 p.
8. **Viljar Palmre.** Fabrication and characterization of microporous carbon-based electroactive polymer actuators. Tartu, 2012, 99 p.
9. **Madis Paalo.** Synthesis of CNT-metal oxide nanocomposites: sol-gel process, rheology, structural and functional properties. Tartu, 2014, 175 p.
10. **Raul Välbe.** Development of ionic liquid composites by sol-gel method for elaboration of industrial nano- and microstructures. Tartu, 2014, 97 p.
11. **Urmas Joost.** Impurity and preparation dependent properties of titania thin films. Tartu, 2014, 155 p.
12. **Madis Umalas.** Application of sol-gel technology for production of ceramic nanocomposites and functional coatings. Tartu, 2015, 136 p.
13. **Elena Samsonova.** Energy transfer probe as a tool to study morphological and structural origins of fluorescence quenching in rare-earth doped nanophosphors. Tartu, 2015, 114 p.
14. **Jay Mondal.** Novel Corrosion Protective Nanostructured Composite Coatings. Tartu, 2016, 104 p.
15. **Kathriin Utt.** Metal oxide mesostructures for optical applications. Tartu, 2016, 88 p.
16. **Kaido Siimon.** Electrospun gelatin cross-linked by glucose. Tartu, 2016, 84 p.
17. **Marko Part.** Combined three-dimensional sol-gel structures and atomic layer deposited thin films. Tartu, 2017, 162 p.
18. **Pejman Rasti.** Analysis of Remote Sensing Image Super Resolution using Fluid Lenses. Tartu, 2017, 188 p.
19. **Ivo Romet.** Recombination luminescence of doped borates: origin and application prospects in dosimetry. Tartu, 2017, 111 p.

20. **Vladimir I. Kondratiev.** Processing and characterization of transparent electrode materials. Tartu, 2017, 111 p.
21. **Taivo Jõgiaas.** Mechanical properties of atomic layer deposited thin films and nanocomposites. Tartu, 2017, 125 p.
22. **Lauri Aarik.** Atomic layer deposition and characterization of thin oxide films for application in protective coatings. Tartu, 2017, 180 p.
23. **Triin Kangur.** Preparation and functional properties of stochastic micro-structured sol-gel silica materials. Tartu, 2018, 96 p.
24. **Marta Berholts.** Fragmentation of ionic and hydrogen-bonded molecules induced by synchrotron radiation. Tartu, 2018, 126 p.
25. **Priit Priimägi.** Development and optimization of 3D-microbatteries. Tartu, 2018, 118 p.
26. **Siim Hödemann.** Residual stress determination in chemically strengthened and thermally tempered glass plates using scattered light method. Tartu, 2019, 146 p.
27. **Jekaterina Kozlova.** Complex characterization of graphene structures on nanometer level. Tartu, 2019, 206 p.
28. **Kristjan Kalam.** Magnetic, electric and structural properties of atomic layer deposited zirconia-based nanolaminates and mixtures. Tartu, 2020, 94 p.
29. **Triinu Vihmann.** Ionic liquids: synthesis and application in lubrication and lithography. Tartu, 2020, 102 p.
30. **Helina Seemen.** Atomic layer deposition and microscopic analysis of magnetically and electrically polarizable thin solid films. Tartu, 2021, 126 p.
31. **Ekaterina Vagapova.** Fluorescence quenching in inorganic crystalline solids activated by neodymium ions; from bulk to micro- and nanocrystals. Tartu, 2021, 116 p.
32. **Evgenii Strugovshchikov.** First-principles studies on rare-earth metal-hydride-based smart materials. Tartu, 2021, 166 p.
33. **Maido Merisalu.** Nanostructured Coatings for Car and Aerospace Industries. Tartu, 2022, 179 p.
34. **Elena Vinogradova.** Optical centers and quantum entangled states of Nd³⁺ ions in doped fluoride crystals. Tartu, 2023, 92 p.